A Numerical Study of Stratified Tidal Rectification over Finite-Amplitude Banks. Part I: Symmetric Banks*

CHANGSHENG CHEN† AND ROBERT C. BEARDSLEY

Department of Physical Oceanography, Woods Hole Oceanographic Institution, Woods Hole, Massachusetts

(Manuscript received 15 April 1993, in final form 6 January 1995)

ABSTRACT

Tidal rectification over a two-dimensional finite-amplitude symmetrical bank is studied using the Blumberg and Mellor primitive equation coastal ocean circulation model (ECOM-si). In the homogeneous case, the nonlinear interaction of tidal currents with the variable bottom topography generates an along-isobath residual circulation over the bank, which tends to increase as either the slope or height of the bank is increased. In the stratified case, internal waves at tidal and higher frequencies are generated over the sloping sides of the bank. Tidal mixing occurs in the bottom boundary layer, leading to horizontal tidal mixing fronts. The resulting stratified tidal rectification associated with the tidal mixing front, the generation of internal tides, and the modification of internal friction due to stratification leads to a subsurface intensification of the along-isobath residual current at the front and at the top of the bottom mixed layer over the slope, and a cross-bank double cell circulation pattern centered at the front near the shelf break. Model results for tidal mixing are in reasonable agreement with a simple energy argument in which the thickness of the tidal mixed layer is proportional to the magnitude of the tidal current and inversely to stratification.

1. Introduction

The basic mechanism of tidal rectification over a variable bottom topography was first studied by Huthnance (1973). Based on a two-dimensional homogeneous fluid model with no along-isobath variation, Huthnance suggested that an along-isobath residual current can be generated against bottom friction by the nonlinear transfer of momentum from the oscillating tidal currents to the mean flow. This mechanism can be alternatively interpreted using a simple vorticity argument. Since the flood tidal current advects negative vorticity to shallow regions and the ebb tidal current advects positive vorticity to deep regions, the net cross-isobath advection of relative tidal vorticity over a tidal cycle can maintain the along-isobath residual flow against friction (Zimmerman 1978, 1980, 1981; Robinson 1981; Maas 1987).

The magnitude and vertical structure of tidally rectified flow depends critically on the horizontal and vertical scales of the bottom topography, the magnitude of the tidal current, friction, and stratification. The residual flow is significant only in the case where the tidal wavelength is much longer than the scale of bottom topography (Loder 1980). The magnitude of the residual flow tends to increase as the bottom slope becomes steeper and the tidal current becomes stronger. Bottom friction is important to balance the net divergence of the across-isobath tidal momentum flux (Loder 1980). Also, friction associated with turbulent mixing in the bottom boundary layer can cause vertical shear and phase shift in the tidal current, which in turn leads to vertically nonuniform momentum transport for both tidal and residual flows (Tee 1979, 1980; Wright and Loder 1985). When stratification is added, the magnitude and vertical structure of the residual current can be modified by a tide-induced front due to turbulent mixing (Loder and Wright 1985), internal tidal generation over the sloping bottom (Maas and Zimmerman 1989a,b), and the modification in internal and bottom friction due to stratification (Loder and Wright 1985; Tee 1985).

Little is known about the influence of tidal mixing and internal tidal generation on stratified tidal rectification over finite-amplitude bottom topography. Garrett and Loder (1981) developed a steady analytically tractable diagnostic model for the quasigeostrophic two-dimensional mean circulation associated with a density front over a sloping bottom in a continuously stratified fluid. This linear model predicts the geostrophic flow along the front driven by the horizontal

* Woods Hole Oceanographic Institution Contribution Number 8214.

† Current affiliation: Department of Marine Sciences, University of Georgia, Athens, Georgia.

Corresponding author address: Dr. Robert C. Beardsley, Department of Physical Oceanography, Woods Hole Oceanographic Institution, Woods Hole, MA 02543.

density gradient and a double cell circulation pattern across the front caused by the pressure gradient force against friction. Coupling linearly the diagnostic frontal model into a depth-dependent tidal model with zero net across-bank transport, Loder and Wright (1985) studied the influence of the density front on the tidally rectified currents over Georges Bank. They found that the along-bank mean flow intensifies at the surface due to the density front and a relatively strong cross-bank double cell circulation occurs on either side of the bank. However, linear superposition of frictionally controlled, tidally rectified and density front-induced currents results in two surface-intensified maximum cores of along-bank mean current on the northern flank of the bank, a prediction which is not supported by observations on the northern side of Georges Bank where the along-bank mean current flows northeastward as a single along-bank jet (Loder et al. 1992). In fact, stratified tidal rectification is an inherently nonlinear problem so that frictional and density-front-induced currents cannot be reproduced in detail through linear superposition.

Maas and Zimmerman (1989a,b) recently investigated tidal rectification associated with internal tidal generation using multiple scale analysis. Based on the different length scales of the barotropic and internal tidal waves, Maas and Zimmerman considered the oscillation of a barotropic tidal current in a linearly stratified fluid over small amplitude bottom topography. This problem is analytically tractable provided that friction is weak and the feedback influence of the residual flow on the tidal flow is ignored. Interaction of a barotropic tidal current over topography in a linearly stratified fluid produces a damped propagating internal tidal wave across the variable bottom topography; the nonlinear interaction between either the barotropic and internal tidal currents or the internal tidal currents themselves then causes a nonpropagating transient, which generates the along- and cross-isobath tidally rectified flow over the topography. Unlike the homogeneous case, the structure of the harmonic and residual currents depends critically on the strength of the stratification. The internal tidal and residual currents are bottom intensified as the internal Rossby deformation radius ($l_i = NH/f$) approaches and exceeds the excursion amplitude of the barotropic tidal current ($l_0 = U/\omega$) or the topographic length scale (l_t). While the Maas and Zimmerman analysis provides a clear picture of some of the physical processes involved in stratified tidal rectification, direct application of their model to study more realistic stratified tidal rectification is not possible due to the limitations of small amplitude topography, weak nonlinearity, and the absence of tidal mixing.

In this paper, we attempt to identify and understand the basic driving mechanisms that occur in stratified tidal rectification over finite-amplitude topography. Since previous work has shown that the dynamical processes will be strongly coupled nonlinearly, we approach this problem numerically and use the primitive equation coastal ocean circulation model developed by Blumberg and Mellor (1987) to obtain solutions in several idealized cases. To better understand the model dynamics and compare with previous theoretical work, we have simplified this initial study to a two-dimensional problem involving a finite-amplitude symmetric bank in which the along-isobath variation for all independent variables is ignored. Since our ultimate objective is to understand stratified tidal rectification over Georges Bank, we pick model parameters for this initial study consistent with Georges Bank. In a subsequent study (Chen et al. 1995), we use this numerical model to study the influence of the asymmetry in the cross-bank topography of Georges Bank on stratified tidal rectification.

This paper consists of seven sections. In section 2, the model is described. In section 3, the results of stratified tidal rectification with different stratification over a finite-amplitude symmetric bank are described and discussed. In section 4, a diagnostic analysis of the momentum and heat balances is made to study the driving mechanisms of homogeneous and stratified tidal rectification over finite-amplitude bottom topography. In section 5, a simple energy argument is used to study tidal mixing and compare with model predictions. The vertical structure of the barotropic and internal tides is described in section 6, and conclusions are given in section 7.

2. The numerical model

The Blumberg and Mellor (1987) model is a three-dimensional Boussinesq, hydrostatic, nonlinear, coastal ocean circulation model. It incorporates the Mellor and Yamada (1982) level 2½ turbulent closure model to provide a realistic parameterization of vertical mixing, and a free surface to simulate surface wave propagation such as tides and long gravity waves. A σ-coordinate transformation is used in the vertical and a curvilinear coordinate system in the horizontal, which allows smooth representation of finite-amplitude bottom topography and variable coastline geometry. Unlike the original Blumberg and Mellor (1987) time-splitting model, a version of their model (called ECOM-si) incorporates a semi-implicit scheme in the horizontal for the barotropic mode, which treats the barotropic pressure gradient in the momentum equations and the velocity convergence in the continuity equation implicitly. This method leads to a linear symmetrical diagonal system at each time step, which can be solved efficiently by a preconditioned conjugate gradient method with no sacrifice in computational time (Casulli 1990). The original 3D model formulation is described in detail by Blumberg and Mellor (1987) and Mellor (1992),

and the semi-implicit version ECOM-si, which we use in this study, is described in detail by Blumberg (1992).[1]

In a system of orthogonal Cartesian coordinates with x increasing northward (in the cross-isobath direction), y increasing westward (in the along-isobath direction), and z increasing upward, the primitive equations in a two-dimensional form with no along-isobath variation ($\partial/\partial y = 0$) are

$$\frac{\partial u}{\partial t} + u\frac{\partial u}{\partial x} + w\frac{\partial u}{\partial z} - fv = -\frac{1}{\rho_0}\frac{\partial P}{\partial x} + \frac{\partial}{\partial z}K_m\frac{\partial u}{\partial z} + F_u, \quad (1)$$

$$\frac{\partial v}{\partial t} + u\frac{\partial v}{\partial x} + w\frac{\partial v}{\partial z} + fu = \frac{\partial}{\partial z}K_m\frac{\partial v}{\partial z} + F_v, \quad (2)$$

$$\frac{\partial P}{\partial z} = -\rho g, \quad (3)$$

$$\frac{\partial u}{\partial x} + \frac{\partial w}{\partial z} = 0, \quad (4)$$

$$\frac{\partial \theta}{\partial t} + u\frac{\partial \theta}{\partial x} + w\frac{\partial \theta}{\partial z} = \frac{\partial}{\partial z}K_H\frac{\partial \theta}{\partial z} + F_\theta, \quad (5)$$

$$\rho_{\text{total}} = \rho_{\text{total}}(\theta, s_0), \quad (6)$$

where u, v, and w are the x, y, and z velocity components, θ the potential temperature, s_0 the reference salinity, p the pressure, f the Coriolis parameter, g the gravitational acceleration, K_m the vertical eddy viscosity coefficient, and K_H the thermal vertical eddy friction coefficient; F_u, F_v, and F_θ represent the horizontal momentum and thermal diffusion terms; and ρ and ρ_0 are the perturbation and reference densities, which satisfy

$$\rho_{\text{total}} = \rho_0 + \rho. \quad (7)$$

To simplify the model problem, we make salinity constant (s_0 = 35 psu) everywhere in the computational domain so that density depends solely on temperature.

The second-order turbulent closure scheme (level 2 1/2) developed by Mellor and Yamada (1974, 1982) is used to close the model problem in which the vertical eddy viscosity and diffusion coefficient are parameterized based on a turbulent kinetic energy and a turbulent macroscale equation. Under the boundary layer approximation where the shear production of turbulent energy can be neglected except in the vertical, the two-dimensional turbulent kinetic energy and turbulent macroscale equations simplify to

$$\frac{\partial q^2}{\partial t} + u\frac{\partial q^2}{\partial x} + w\frac{\partial q^2}{\partial x} = 2(P_s + P_b - \epsilon) + \frac{\partial}{\partial z}\left(K_q\frac{\partial q^2}{\partial z}\right) + F_q, \quad (8)$$

$$\frac{\partial q^2 l}{\partial t} + u\frac{\partial q^2 l}{\partial x} + w\frac{\partial q^2 l}{\partial z} = lE_1\left(P_s + P_b - \epsilon\frac{W}{E_1}\right) + \frac{\partial}{\partial z}\left(K_q\frac{\partial q^2 l}{\partial z}\right) + F_l, \quad (9)$$

where $q^2/2 = \frac{1}{2}(u'^2 + v'^2)$ is the turbulent kinetic energy, l the turbulent macroscale, K_q the eddy diffusion coefficient of the turbulent kinetic energy, and F_q and F_l represent horizontal diffusion of the turbulent kinetic energy and macroscale; P_s and P_b are the shear and buoyancy productions of turbulent energy, defined as

$$P_s = K_M\left[\left(\frac{\partial u}{\partial z}\right)^2 + \left(\frac{\partial v}{\partial z}\right)^2\right], \quad P_b = \frac{g}{\rho_0}K_H\frac{\partial \rho}{\partial z}; \quad (10)$$

ϵ is the turbulent energy dissipation given by $\epsilon = q^3/(B_1 l)$, W a wall proximity function defined as $W = 1 + E_2(l/\kappa L)^2$, $(L)^{-1} = (\eta - z)^{-1} + (H + z)^{-1}$, κ the von Kármán constant, H the water depth, η the free surface elevation, and E_1, E_2, and B_1 are empirical constants. Parameterization has been made for vertical turbulent momentum and heat fluxes in the model where the vertical fluxes of horizontal turbulent momentum $-\langle w'u'\rangle$ and $-\langle w'v'\rangle$ are expressed in terms of the product of vertical eddy viscosity and vertical shear of the horizontal velocity, and the vertical heat flux $-\langle \theta'w'\rangle$ is given in terms of the product of vertical thermal diffusion coefficient and vertical density gradient. A small amount of horizontal diffusion is retained to help ensure numerical stability: for homogeneous experiments, the horizontal diffusion coefficients are set equal to 1 $m^2\ s^{-1}$, while for experiments with stratification, the coefficients equal 20 $m^2\ s^{-1}$.

The turbulent kinetic energy and macroscale equations are closed by defining

$$K_M = lqS_M, \quad K_H = lqS_H, \quad K_q = 0.2lq, \quad (11)$$

where S_M and S_H are stability functions given by

$$S_M = \frac{C_{22}D_1 + C_{12}D_2}{C_{11}C_{22} + C_{12}C_{21}}, \quad S_H = \frac{C_{21}D_1 - C_{11}D_2}{C_{11}C_{22} + C_{12}C_{21}}, \quad (12)$$

[1] This work was started before the final version of ECOM-si was developed, and we did not incorporate the Galperin et al. (1988) modification of the stability functions, which are now included in ECOM-si as described by Blumberg (1992). After this work was completed, we reran several experiments to determine if the Galperin et al. (1988) modifications made much difference in our results and concluded that the primary results presented in this paper are robust and the locations of the tidal mixing front and associated residual currents do not depend significantly on which stability functions are used. We did find, however, that the rate of tidal mixing depends on the choice of stability functions and, to a lesser extent, the vertical grid resolution. With the Galperin et al. (1988) modifications, the time interval required for the bottom mixed layer to reach a quasi equilibrium was increased [the results presented in section 5 were obtained with the Galperin et al. (1988) modifications].

where

$$C_{11} = 6A_1A_2G_M,$$
$$C_{12} = 1 - (2A_2B_2 - 12A_1A_2)G_H, \quad D_1 = A_2,$$
$$C_{21} = 1 + 6A_1^2G_M - 9A_1A_2G_H,$$
$$C_{22} = (12A_1^2 + 9A_1A_2)G_H, \quad D_2 = A_1(1 - 3C_1),$$

and

$$G_M = \frac{l^2}{q^2}\left[\left(\frac{\partial u}{\partial z}\right)^2 + \left(\frac{\partial v}{\partial z}\right)^2\right], \quad G_H = \frac{l^2}{q^2}\left(\frac{g}{\rho_0}\frac{\partial \rho}{\partial z}\right).$$

With the empirical constants given, the stability functions are determined by solving a linear algebraic equation and the solutions depend on the vertical shear of mean flow and stratification. All empirical constants mentioned above have been assigned by Mellor and Yamada (1982) based on laboratory experiments; they are

$$(A_1, A_2, B_1, B_2, C_1, E_1, E_2) = (0.92, 0.74, 16.6, 10.1, 0.08, 1.8, 1.33). \quad (13)$$

In the absence of wind stress and surface and bottom heat fluxes, the surface and bottom boundary conditions are

$$\left.\begin{aligned} &\frac{\partial u}{\partial z} = \frac{\partial v}{\partial z} = \frac{\partial \theta}{\partial z} = 0 \\ &q^2 = q^2 l = 0 \\ &w = \frac{\partial \eta}{\partial t} + u\frac{\partial \eta}{\partial x} \end{aligned}\right\} \quad \text{at} \quad z = \eta(x, t)$$

and

$$\left.\begin{aligned} &K_M\left(\frac{\partial u}{\partial z}, \frac{\partial v}{\partial z}\right) = \left(\frac{\tau_{bx}}{\rho_0}, \frac{\tau_{by}}{\rho_0}\right) \\ &q^2 = B_1^{2/3}u_{\tau b}^2 \\ &q^2 l = \frac{\partial \theta}{\partial z} = 0 \\ &w = -u\frac{\partial H}{\partial x} \end{aligned}\right\} \quad \text{at} \quad z = -H(x),$$

where τ_{bx} and τ_{by} are the x and y components of bottom stress, and $u_{\tau b}$ the friction velocity associated with the bottom stress. The bottom stress is determined by matching a logarithmic bottom layer to the model at a height z_{ab} above the bottom so that

$$(\tau_{bx}, \tau_{by}) = C_d\sqrt{u^2 + v^2}(u, v), \quad (14)$$

where

$$C_d = \max\left(\frac{\kappa^2}{\ln(z_{ab}/z_0)^2}, 0.0025\right), \quad (15)$$

and z_0 is the bottom roughness parameter, taken here as $z_0 = 0.001$ m.

The numerical model domain is shown in Fig. 1. The depth distribution of the symmetrical bank is expressed analytically by

$$h(x) = \begin{cases} H_d, & x \le x_{c_1} \\ \frac{1}{2}(H_d + H_s) + \frac{1}{2}(H_d - H_s)\cos\left(\frac{\pi(x - x_{c_1})}{x_{s_1} - x_{c_1}}\right), & x_{c_1} \le x \le x_{s_1} \\ H_s, & x_{s_1} \le x \le x_{s_2} \\ \frac{1}{2}(H_d + H_s) + \frac{1}{2}(H_d - H_s)\cos\left(\frac{\pi(x - x_{c_2})}{x_{c_2} - x_{s_2}}\right), & x_{s_2} \le x \le x_{c_2} \\ H_d, & x_{c_2} \le x, \end{cases}$$

where $h(x)$ is the height of the bank, and H_s and H_d are the water depths over the flat top of the bank and in the deep region away from the bank, respectively. This formula was first used by Loder (1980) in his barotropic model to provide a smooth bottom topography with continuous first derivatives $h'(x)$ across the bank. The water depth in our numerical experiments is chosen as 300 m in the deep region away from the bank and 100 or 50 m over the top of the bank.

The numerical model uses the σ-coordinate transformation $\sigma = (z - \eta)/(H + \eta)$ to map the bank topography into a flat-bottom domain, where σ varies from 0 at the free surface to -1 at the bottom; σ is discretized with a uniform grid. The number of σ grid points is chosen as $KB = 31$ ($\Delta\sigma = 1/(KB - 1) = 0.033$) in order to provide good resolution of the bottom boundary layer transport (Chen 1992), while minimizing the finite-difference error in the baroclinic pressure gradient over steep topography (see the appendix). The matching height for the bottom log layer in (16) is taken as $z_{ab} = z(KB - 1) - z(KB)$.

The numerical model domain incorporates nonuniform horizontal resolution. A fine grid with increment Δx_1 is taken across and near the bank, with a linearly increasing function used to connect it to a coarse grid with increment Δx near the open boundary.

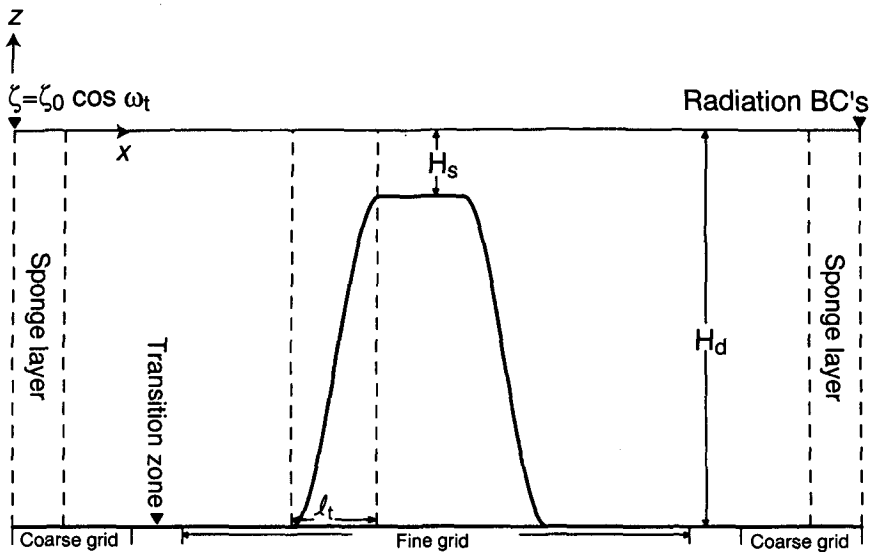

FIG. 1. Numerical model domain: ζ is the free surface, ζ_0 the amplitude of the M_2 tidal wave at the upstream boundary, ω the M_2 tidal frequency, and H_s and H_d the water depths on and off the bank. The bank is symmetric about its center; l_t is the topographic scale. Due to our ultimate objective of applying this model to Georges Bank, we will refer to the upstream boundary at $x = 0$, where the tidal forcing is imposed as the southern boundary and the downstream boundary as the northern boundary.

The advantage of this nonuniform grid is to filter out short internal waves propagating toward the open boundaries without losing horizontal resolution near the bank, thus reducing the strength of the artificial sponge layer used at the open boundaries. In our experiments, Δx is taken as 11.96 km, and Δx_1 is 2.5 km for homogeneous cases and 1.25 km for stratified cases. The model time step is 110.4 sec based on the condition of minimum reflection from the open boundary ($\sqrt{gH_d}\,\Delta t/\Delta x = 0.5$, Chapman 1985).

The model is forced by the barotropic M_2 tide (with an amplitude $\zeta_0 = 0.5$ m) at the upstream boundary (which we will call the southern boundary). Also, a gravity wave radiation boundary condition (with a propagation speed of $\sqrt{gH_d}$) is specified at the downstream (northern) boundary to allow the tidal wave to propagate out of the computational domain with minimum reflection (see Chapman 1985 for a comprehensive discussion). Since the radiation boundary condition in the finite-difference scheme only allows the barotropic tidal wave to travel out of the computational domain, we add a sponge layer near each open boundary to absorb the internal waves propagating toward the boundary.

The model has been run with homogeneous, weak and strong stratification over a finite-amplitude symmetric bank. Initial temperature distributions for weak and strong stratification cases are given by simple linear functions of z based on observations made across Georges Bank during winter and summer 1979 (Flagg 1987). The initial surface and bottom (at a depth of 300 m) temperatures are taken as 20° and 11°C for the strong stratification case and 13° and 11°C for the weak stratification case. The initial Brunt–Väisälä frequency N is equal to 10^{-2} s^{-1} (3×10^{-3} s^{-1}) in the strong (weak) stratification cases. To avoid transients due to sharp initial conditions, we ramp up the model tidal forcing from zero to full value over one and one-half days. Once the tidal currents reach a quasi-equilibrium state (Chen 1992), the residual flow and mean temperature fields are obtained by averaging over one tidal cycle.

3. The model results

a. Along-isobath residual flow and mean temperature structure

Figure 2 shows the structure of along-isobath residual current ($\bar{v}$) and mean temperature ($\bar{T}$) for different stratification cases across a finite-amplitude symmetric bank with $l_t = 50$ km and $H_s = 100$ m. In the homogeneous fluid case (Fig. 2a), the model predicts a topographically controlled, surface-intensified jetlike along-isobath residual current on both sides of the bank with a maximum velocity of about 2.4 cm s^{-1} near the shelf break. In our model domain, the along-isobath flow is positive toward the (west) along the southern side of the bank and negative (toward the east) along the northern side, consistent with the general prediction of homogeneous tidal rectification of clockwise flow around elongated east–west banks in the Northern Hemisphere. In the weak stratification case with N

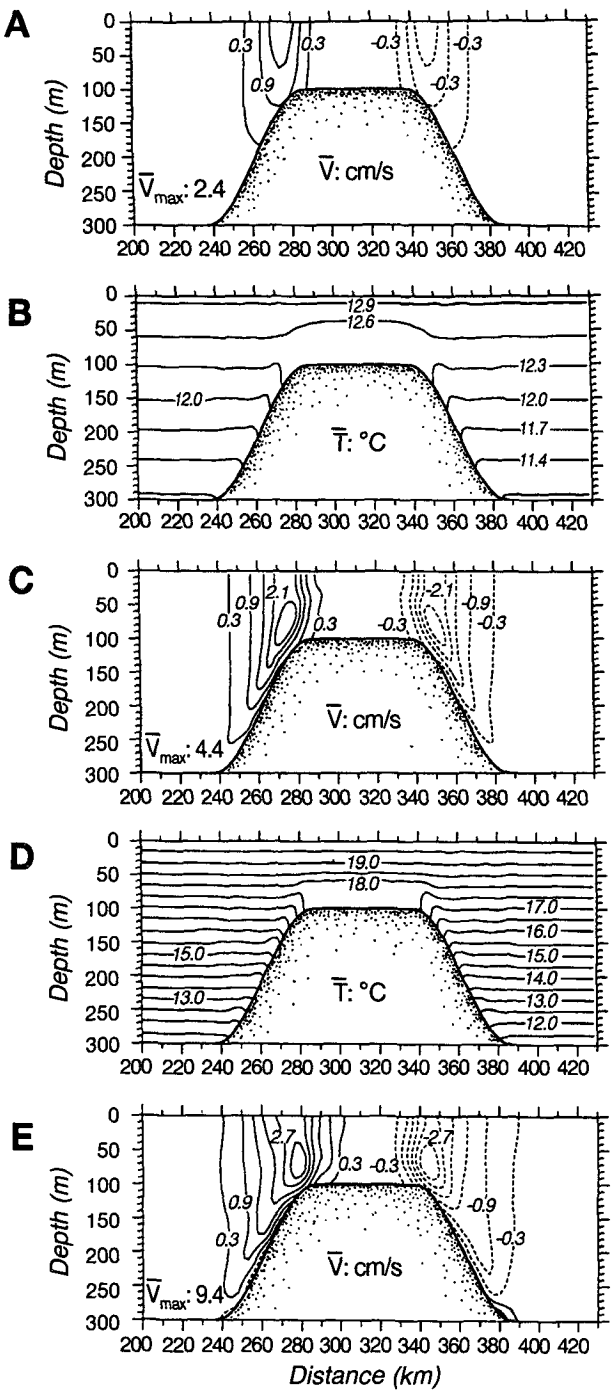

FIG. 2. Structure of along-isobath residual current ($\bar{v}$) and mean temperature ($\bar{T}$) for the (a) homogeneous, (b and c) weak, and (d and e) strong stratification cases. The water depth H_s = 100 m over the bank, and H_d = 300 m away from the bank. The topographic scale l_t = 50 km. The contour interval is 0.6 cm s^{-1} for the residual current and 0.3° and 0.5°C for mean temperature in the weak and strong stratification cases, respectively. The value at the left lower corner in each current figure is the maximum velocity. (Note: The maximum velocity is not contoured in this figure due to lack of resolution in the contouring program.)

= 3×10^{-3} s^{-1} (Figs. 2b,c), turbulent mixing associated with relatively strong tidal currents results in a mixed layer about 60 m thick above the bottom over the bank and hence creates the tidal mixing fronts near the shelf break on both sides of the bank. Next to this front, tidal mixing plus thermal diffusion also generates a bottom mixed layer over the slope, thinner in the deep region and thicker as the water becomes shallower. As a result, the along-isobath residual current intensifies at the front with a maximum of about 4.4 cm s^{-1} at a height of 30 m above the bottom, and the axis of the strongest currents coincides with the top of the bottom boundary layer over the upper slope. When stratification is increased to $N = 10^{-2}$ s^{-1} (Figs. 2d,e), tidal mixing is reduced and hence the thickness of the bottom mixed layer decreases to 40 m over the top of the bank. Although the structure of the along-isobath residual current remains almost unchanged, the strength of this current intensifies as stratification increases. The maximum velocity is found to be 9.4 cm s^{-1} at the front at a height of 20 m above the bottom, about four times as large as that in the homogeneous case and about twice as large as that in the weak stratification case. The horizontal scale of the along-isobath residual flow (i.e., the width of the current greater than 0.3 cm s^{-1}) on either side of the bank tends to be wider as stratification increases. It is about 35 km in the homogeneous case but increases to 45 km in the weak stratification case and 60 km in the strong stratification case. The offbank decay distance of this current is about 20 km in the homogeneous case but about 30 and 40 km in the weak and strong stratification cases, respectively. The decay scale of the current in the stratified cases seems not to be controlled strictly by the internal Rossby deformation radius [$l_i = NH_d/f = 10$ (weak stratification case) or 30 km (strong stratification case)].

The model was also run with different topographic slopes (l_t = 25 and 12.5 km) and heights of the bank (H_s = 50 m) to investigate the dependence of tidal mixing and residual flow on bottom topography. As an example, Fig. 3 shows the structure of along-isobath residual current and mean temperature for different stratification with l_t = 50 km and H_s = 50 m. As H_s decreases from 100 to 50 m, mass conservation results in increased barotropic tidal currents over the bank, with maximum velocities of 70 cm s^{-1} in u and 50 cm s^{-1} in v, about 15–20 cm s^{-1} larger than when H_s = 100 m. As a result, the maximum along-isobath residual flow in the homogeneous case increases to 7 cm s^{-1}, even though the structure of this flow remains unchanged (Fig. 3a). The stronger tidal currents also cause increased turbulent mixing that mixes the whole water column over the top of the bank, creating the well-defined symmetric thermal fronts at the 78-m isobath in the weak stratification case (Fig. 3b) and at the 56-m isobath in the strong stratification case (Fig. 3d).

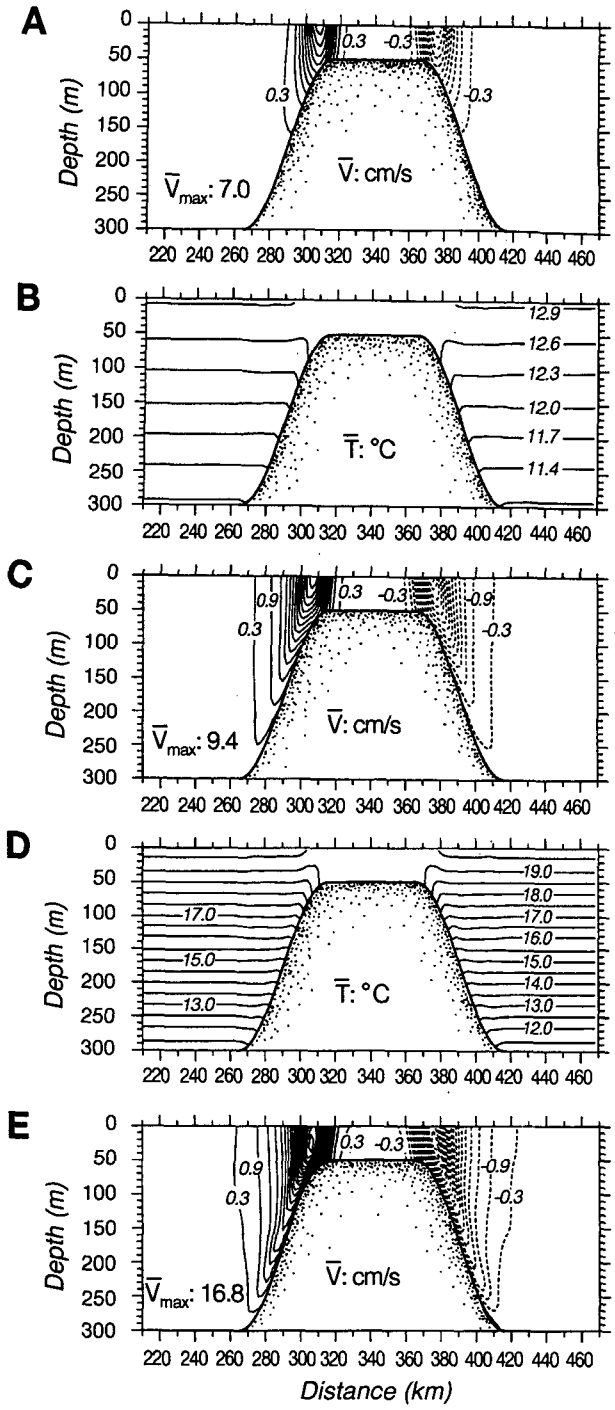

FIG. 3. Structure of along-isobath residual current ($\bar{v}$) and mean temperature ($\bar{T}$) for the (a) homogeneous, (b and c) weak, and (d and e) strong stratification cases. The water depth H_s = 50 m over the bank and H_d = 300 m away from the bank. The topographic scale l_t = 50 km. The contour interval is 0.6 cm s^{-1} for residual currents and either 0.3° or 0.5°C for mean temperature in the weak and strong stratification cases. The value at the left lower corner in each current figure is the maximum velocity. (Note: The maximum velocity is not contoured in this figure due to lack of resolution in the contouring program.)

As a result, the along-isobath residual current intensifies at the front with a maximum velocity of either 9.4 cm s^{-1} at the surface in the weak stratification case (Fig. 3c) or 16.8 cm s^{-1} at a depth of about 20 m from the surface in the strong stratification case (Fig. 3e). The cross-isobath scale of along-isobath residual flow remains unchanged for homogeneous, weak and strong stratified cases as the height of the bank is increased. This result implies that the horizontal scale of the tidal-rectified flow is independent of the height of the bank. In addition, the numerical experiments with different topographic scales show that steepening the bottom slope does not change the thickness of the tidal mixed layer over the bottom, even though it does tend to strengthen the residual flow and decrease the cross-isobath motion scale in the homogeneous case (Chen 1992).

b. Cross-isobath residual flow and mean surface elevation structure

Figure 4 shows the distribution of the mean surface elevation ($\bar{\zeta}$), cross-isobath residual current ($\bar{u}$), and the vertical residual velocity ($\bar{w}$) in the strong stratification case with H_s = 50 m and l_t = 50 km (corresponding to Figs. 3d,e). A relatively strong cross-isobath double cell circulation pattern is found on both sides of the bank where the water tends to be upwelled to the surface along the bottom slope and the axis of maximum horizontal gradient of temperature and then downwelled on both sides of the front (Fig. 4b), causing convergence near the bottom and divergence near the surface (Fig. 4c). The maximum vertical velocity is about 3×10^{-2} cm s^{-1} in the upwelling region and about 5×10^{-3} cm s^{-1} in the downwelling region, corresponding to a cross-isobath current of about 2.0 cm s^{-1} near the surface and bottom at the front. A very smooth and large gradient of mean surface elevation is observed across the bank, which results in a barotropic along-isobath geostrophic mean current of about 4.3 cm s^{-1} where the upwelling is strongest (Fig. 4a). This barotropic current accounts for almost one-fourth of the total along-isobath residual current, implying that the surface pressure gradient is important in the momentum balance in stratified tidal rectification. The structure of the cross-isobath residual current and mean surface elevation in the weak stratification case (not shown) is similar except for the weaker magnitudes in the currents and the mean surface elevation. The maximum vertical velocity is about 5.0×10^{-3} cm s^{-1} in the upwelling region and 1.0–2.0 ($\times 10^{-3}$ cm s^{-1}) in the downwelling region, which corresponds to a cross-isobath horizontal velocity of about 1.0 cm s^{-1} at the surface and 0.5 cm s^{-1} near the bottom (Chen 1992). The maximum horizontal surface pressure gradient is about 1.9×10^{-7} over the slope, resulting in an along-isobath barotropic current of about

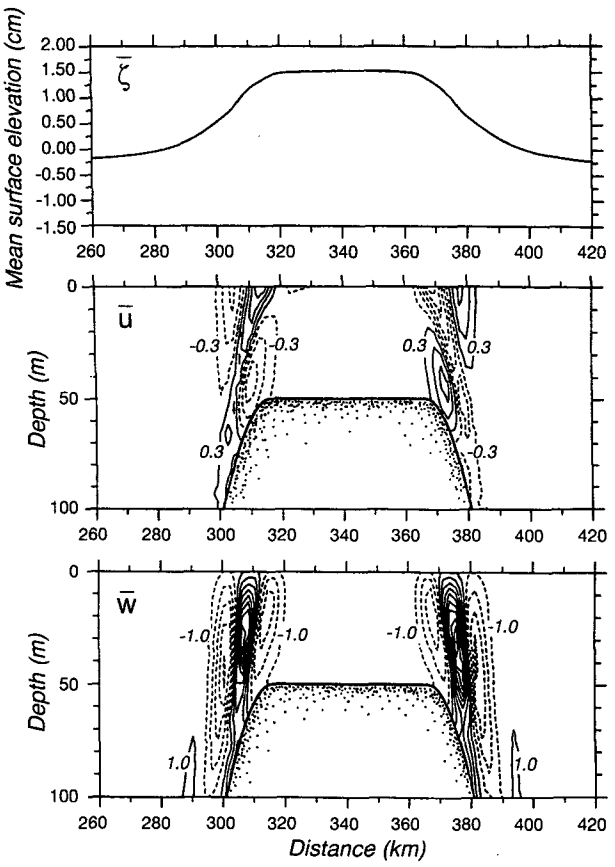

FIG. 4. Distribution of mean surface elevation ($\bar{\zeta}$), cross-isobath residual velocity ($\bar{u}$), and vertical residual velocity ($\bar{w}$) for the strong stratification case. The water depth H_s = 50 m over the bank and H_d = 300 m away from the bank. The topographic scale l_t = 50 km. The contour interval is 0.6 cm s^{-1} for the cross-isobath residual current and 1 × 10^{-3} cm s^{-1} for the vertical residual velocity.

1.8 cm s^{-1}, 2.5 cm s^{-1} smaller than that in the case of strong stratification.

Unlike the stratified cases, two minima in mean sea level elevation are found near the points of maximum along-isobath residual flow in the homogeneous case, which correspond to a maximum horizontal divergence in the cross-isobath residual current (Chen 1992). However, the strength of the cross-isobath currents and the mean surface elevation is much smaller than those in the stratified cases. For example, in the case of H_s = 50 m and l_t = 50 km, the maximum of cross-isobath residual flow is only about 0.1 cm s^{-1} in $\bar{u}$ and less than 10^{-3} cm s^{-1} in $\bar{w}$. The cross-isobath gradient of mean surface elevation is about 0.5 × 10^{-7} over the slope, which can only generate an along-isobath geostrophic velocity of about 0.5 cm s^{-1}, which is only 7% of the total along-isobath mean current.

c. *Comparison with previous analytical models*

Model results in the homogeneous case obtained in these numerical experiments are qualitatively consistent with analytical solutions from either simplified depth-averaged models (Loder 1980; Zimmerman 1978, 1980) or depth-dependent models (Wright and Loder 1985; Tee 1985, 1987). Based on the harmonic truncation method, Loder (1980) analytically predicted a clockwise-like residual circulation over Georges Bank with a maximum near the shelf break and decaying exponentially away from the bank. Young (1983) and Maas et al. (1987) separately used second-order momentum and spectral theories to argue that the residual flow should be a jetlike circulation limited over the bank. Our numerical results show an along-isobath residual circulation over a finite-amplitude symmetrical bank, which is in good agreement with their theories. A friction-induced, double cell, cross-isobath mean circulation over Georges Bank was predicted by Loder and Wright (1985) with a depth-dependent and constant vertical eddy viscosity model. A similar structure was found numerically by Tee (1987) with a no-slip bottom boundary condition. This is also true in our model results where a double cell cross-isobath circulation pattern is centered at the shelf break on both sides of the bank.

Our model results with stratification are similar in some aspects to previous theoretical work. Based on the depth-dependent tidal rectified model with a linear density front, Loder and Wright (1985) predicted a relatively strong cross-bank double cell circulation on either side of Georges Bank due to the density front. A similar structure was also found by Maas and Zimmerman (1989b) at the point of maximum along-isobath residual flow in an internal tidal model over small-amplitude bottom topography where no tidal mixing was included. Our numerical model does show a similar structure over a finite-amplitude symmetric bank in both weak and strong stratification cases. Unlike earlier work, however, our model with stratification includes three driving mechanisms: 1) a tide-induced front due to turbulent mixing, 2) internal tide generation over the slope, and 3) modified internal and bottom friction due to stratification. The nonlinear coupling of these three factors results in a single maximum core of along-isobath residual flow over each side of the bank. In addition, numerical experiments with different stratification over different bank topographies allow a detailed quantitative analysis of the effects of stratification and bottom topography on tidal mixing and stratified tidal rectification, which is not possible in existing analytical models.

4. Diagnostic analysis for momentum and heat balances

To better understand the driving mechanisms of stratified tidal rectification over large topography, we have made diagnostic computations for each term in the momentum equations for both the homogeneous

and strong stratification cases. As an example, Figs. 5 and 6 show the time series of each term in the momentum equations at $\sigma = -0.033$ (near the surface) and -0.9 (near the bottom) at the 127-m isobath on the slope for the homogeneous and strong stratification cases with $H_s = 50$ m and $l_t = 50$ km (corresponding to Fig. 3). Figure 7 shows each thermodynamic term in the temperature equation at the same depths for the strong stratification case.

a. Momentum and heat balances of tidal flow

In the homogeneous case (Fig. 5), the tidal momentum balance is characterized by the inertial–gravity wave equations in which the local acceleration term is balanced principally by the sum of the Coriolis and pressure gradient terms in the cross-isobath direction and by the Coriolis term in the along-isobath direction. Nonlinear advection terms behave as a first-order modification for the inertial–gravity wave on the slope and increase as the water depth becomes shallower, reaching a maximum near the shelf break where the strongest along-isobath residual current is located. The vertical friction term is, in general, one order of magnitude smaller than the Coriolis term and is only distinguishable near the bottom.

In the strong stratification case (Figs. 6, 7), the tidal momentum balance is similar to that in the homogeneous case near the surface, but it is very complex near the bottom. Time series of each term in the momentum equations are significantly different near the bottom between periods of flood (onbank current) and ebb (offbank current) tides. The vertical friction term gradually increases as the tide floods onto the bank and

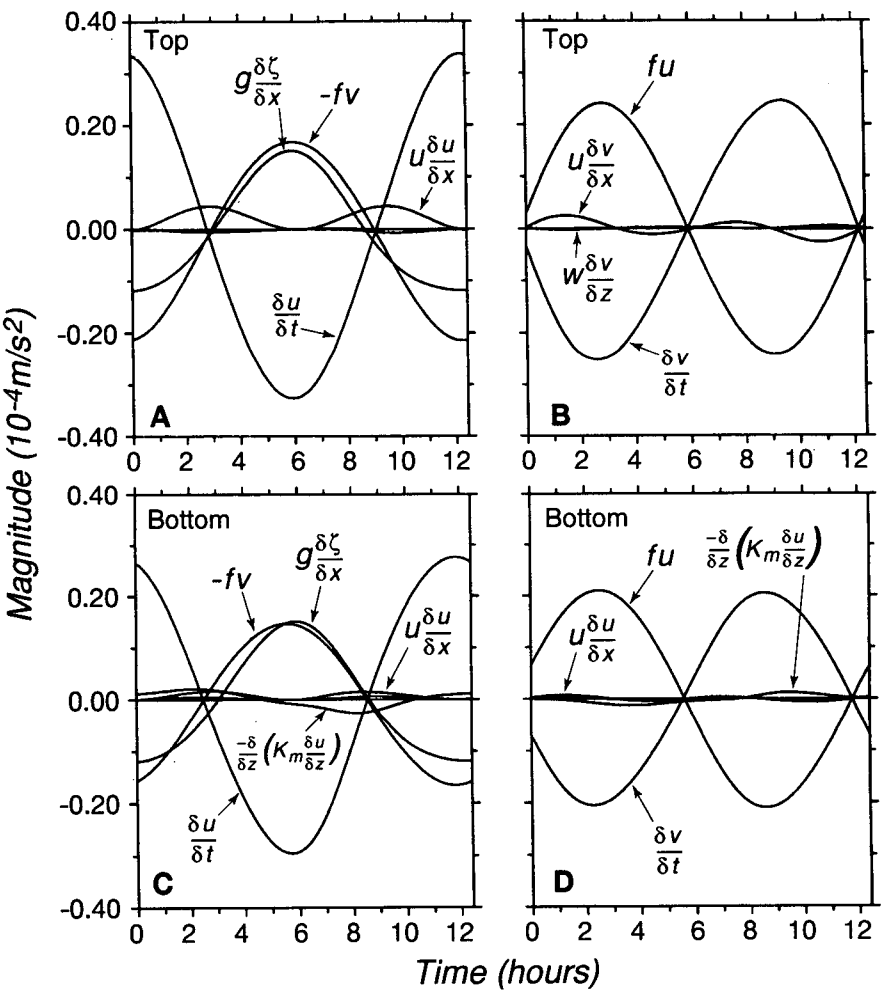

FIG. 5. Time series of terms in the momentum equations at $\sigma = -0.033$ near the surface (a and b) and $\sigma = -0.9$ near the bottom (c and d) at the 127-m isobath over the slope for the homogeneous case with $H_s = 50$ m and $l_t = 50$ km (Fig. 3a). Terms not shown in each panel are significantly smaller than 10^{-6} m s^{-2}.

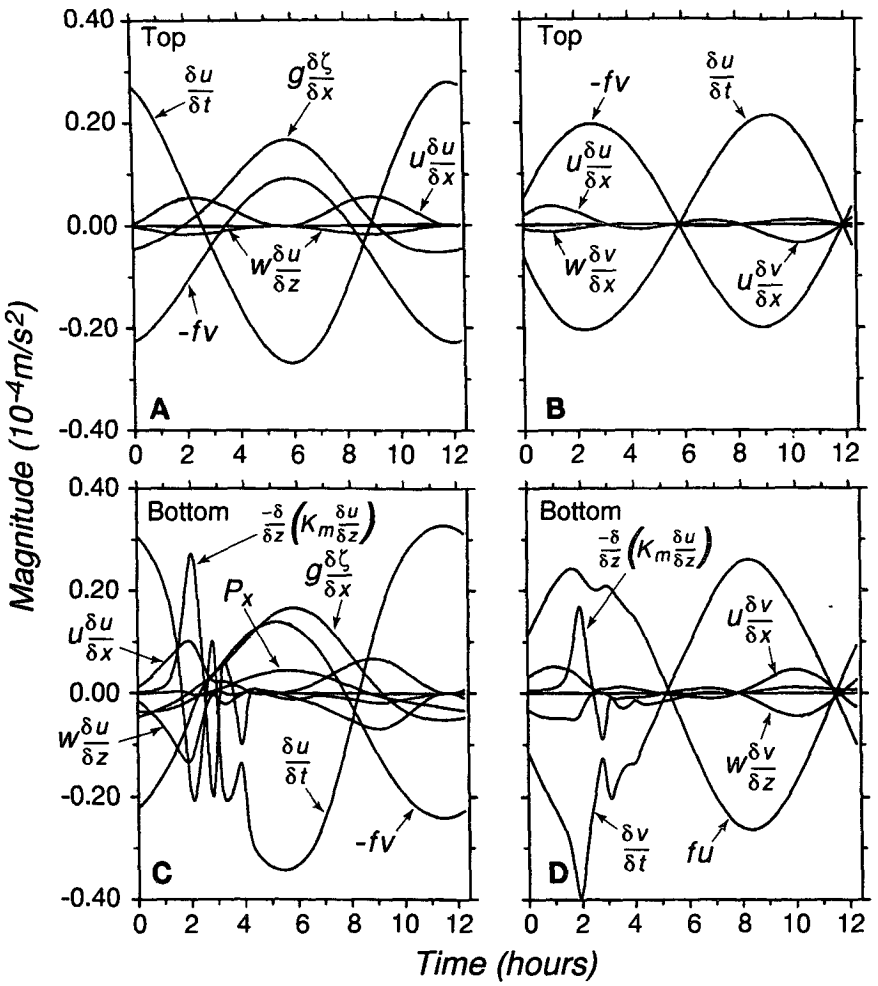

FIG. 6. Time series of terms in the momentum equations at $\sigma = -0.033$ near the surface (a and b) and at $\sigma = -0.9$ near the bottom (c and d) at the 127-m isobath over the slope for the strong stratification case with $H_s = 50$ m and $l_t = 50$ km (Figs. 3d,e). Terms not shown in each panel are significantly smaller than 10^{-6} m s^{-2}.

reaches a maximum after the maximum tide occurs, causing a high-frequency internal wave borelike structure in u (Fig. 6c) and a small peak in T (Fig. 7b). The period of this fluctuation is about 3 hours; it damps very rapidly as the flood tide weakens and then returns to the modified inertial-gravity wave equations similar to the upper layer during the ebb tide. Since the horizontal and vertical momentum fluxes tend to cancel each other during the tidal period over the slope, the vertical viscosity term may be responsible for the generation of the high-frequency internal wave bore. The vertical eddy viscosity K_m is significantly larger during the flood tide period but rapidly decays with a damped oscillation as the tidal current ebbs (Chen 1992), suggesting that the turbulence-induced friction plays an important role in dissipating the energy of the internal wave bore. In addition, the horizontal temperature advection term is always opposite to the vertical temperature advection term over the slope. These two terms tend to cancel each other and the residue is generally balanced by the vertical thermal diffusion, resulting in a small local time variation of temperature over the slope (Figs. 7a,b).

b. Momentum and heat balances of residual flow

Cross-bank distributions of significant dynamical terms averaged over a tidal cycle in the momentum equations for the case of $H_s = 50$ m and $l_t = 50$ km are plotted in Fig. 8 for the homogeneous case. Unlike the vertically averaged model where the cross-isobath mean current is assumed to be zero (Loder 1980), the Coriolis force becomes relatively important in the along-isobath momentum balance and adds together

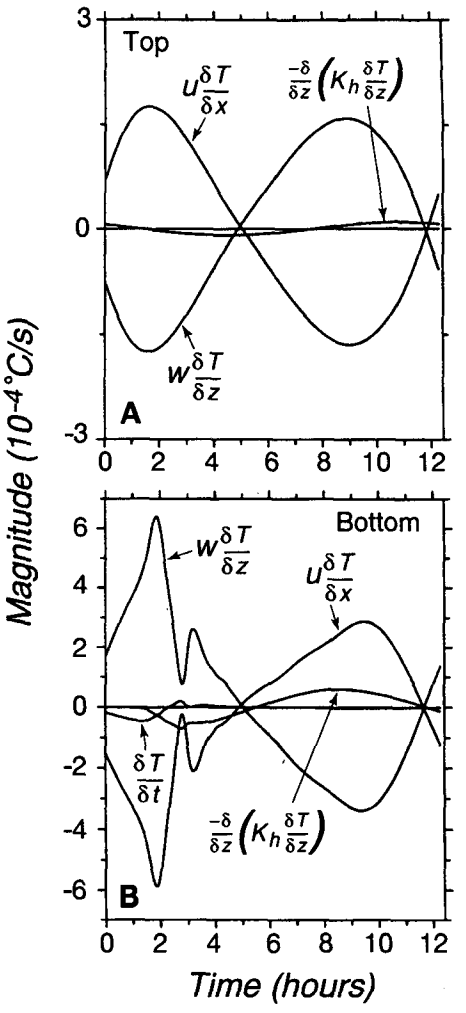

FIG. 7. Time series of terms in the heat equation at $\sigma = -0.033$ near the surface (a) and $\sigma = -0.9$ near the bottom (b) at the 127-m isobath over the slope for the strong stratification case with $H_s = 50$ m and $l_t = 50$ km (Figs. 3d,e). Terms not shown in each panel are significantly smaller than 10^{-6} °C s^{-1}.

with the horizontal advection to balance the vertical friction. The basic balance in the cross-isobath direction is between the horizontal advective and Coriolis terms. The cross-isobath gradient of mean surface elevation is, in general, one order smaller than the horizontal advective term except at the edge of the bank, 7 km away from the core of maximum along-isobath residual current where the residual current is relatively small. In summary, the basic momentum balance for the mean flow in the homogeneous case is given by

$$\overline{u\frac{\partial u}{\partial x}} - f\bar{v} = -g\overline{\frac{\partial \zeta}{\partial x}} \tag{16}$$

$$\overline{u\frac{\partial v}{\partial x}} + f\bar{u} = \overline{\frac{\partial}{\partial z}K_m\frac{\partial v}{\partial z}}, \tag{17}$$

where the cross-isobath gradient of mean surface elevation is, in general, one order smaller than the other terms in the equation. These balance relations indicate a simple driving mechanism by which the along-isobath mean flow is generated through the momentum transfer from tidal currents to mean flow against friction. The flow reaches its steady state when the Coriolis force term is balanced by the nonlinear advection term in the cross-isobath direction and by the nonlinear advection and vertical friction terms in the along-isobath direction.

Cross-bank distributions of the significant dynamical and thermodynamical terms averaged over a tidal cycle in the momentum and heat equations for the strong stratification case are shown in Figs. 9 and 10. Unlike the homogeneous case, all the dynamic terms except the cross-isobath vertical friction become important in the cross- and along-isobath momentum balances over finite-amplitude bottom topography in the strong stratification case. In the cross-isobath direction, the horizontal advection term, which is significant only in the upper 150 m near the shelf break and is surface intensified in the homogeneous case, extends downward along the slope to the edge of the bottom topography and has a maximum at a depth of about 20 m near the tidal front. Associated with increasing stratification, the vertical advection term becomes larger, with a negative extreme near the surface but positive maximum near the bottom, just like a first baroclinic mode. The tidal mixing front creates a core of maximum cross-isobath baroclinic pressure gradient centered at a depth of about 70 m and 10 km away from the shelf break. This pressure gradient and the horizontal and vertical advection intensify the along-isobath residual current at the subsurface and over the slope.

In the along-isobath direction, the horizontal and vertical advection terms, which are relatively weak and surface intensified in the homogeneous case, are considerably increased as strong stratification is included and are mainly characterized by a first baroclinic mode in the vertical. Associated with these vertical distributions of the nonlinear terms, the cross-isobath current diverges at the front and converges on both sides of the front near the surface and reverses near the bottom, resulting in a cross-isobath double cell circulation pattern centered at the front near the shelf break. The mean temperature balance is relatively simple at tidal mixing fronts. Since vertical thermal diffusion is in general one or two orders of magnitude weaker than the advection terms in the heat equation, the mean temperature field is maintained through a basic balance between horizontal and vertical temperature advection. In summary, the basic momentum and heat balances in the form of mean equations for stratified tidal rectification are given by

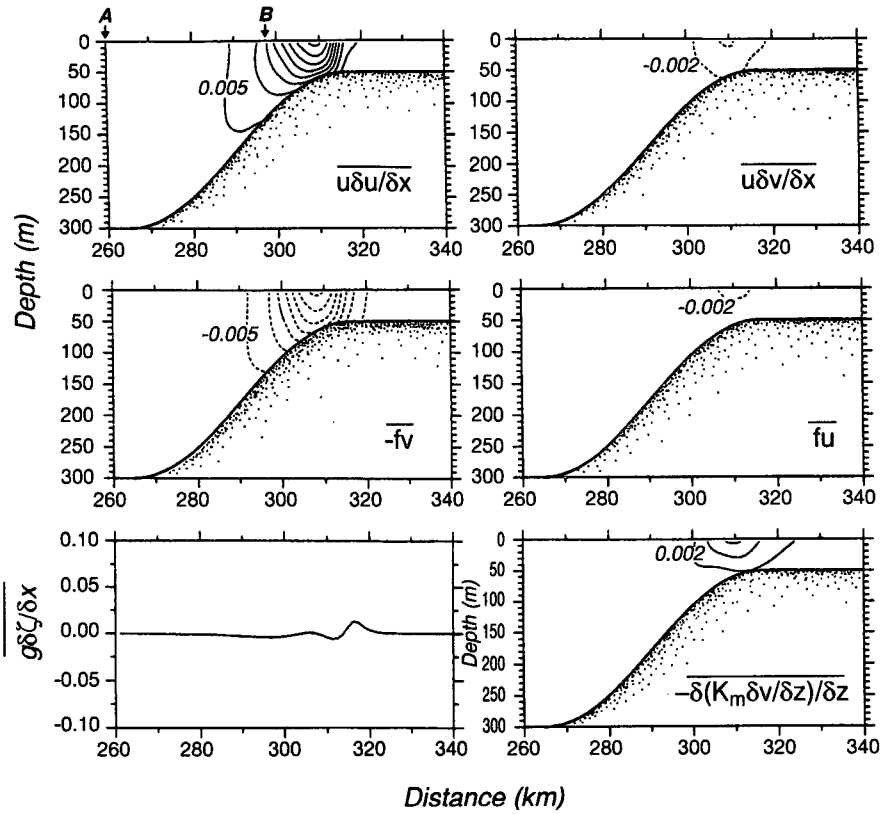

FIG. 8. Cross-bank distribution of terms averaged over one tidal cycle in the cross- and along-bank momentum equations for the homogeneous case with H_s = 50 m and l_t = 50 km (Fig. 3a). The unit is 10^{-4} m s^{-2}, and the contour interval is 0.005 × 10^{-4} m s^{-2} for terms in the along-bank momentum equation and 0.01 × 10^{-4} m s^{-2} for terms in the cross-bank momentum equation.

$$\overline{u\frac{\partial u}{\partial x}} + \overline{w\frac{\partial u}{\partial z}} - f\bar{v} \sim -g\frac{\partial \bar{\zeta}}{\partial x} - \overline{P_x}, \qquad (18)$$

$$\overline{u\frac{\partial v}{\partial x}} + \overline{w\frac{\partial v}{\partial z}} + f\bar{u} \sim \overline{\frac{\partial}{\partial z}K_m\frac{\partial v}{\partial z}}, \qquad (19)$$

$$\overline{u\frac{\partial T}{\partial x}} + \overline{w\frac{\partial T}{\partial z}} \sim 0. \qquad (20)$$

c. *Driving mechanisms of stratified tidal rectification*

Figure 11 shows the mean eddy viscosity $\bar{K}_m$ at the 67-m isobath near the shelf break (H_s = 50 m) for homogeneous, weak and strong stratification cases. In the homogeneous case, the predicted $\bar{K}_m$ is characterized by a parabolic curve in the vertical, with a maximum of 0.05 m^2 s^{-1} near midwater depth. As weak stratification is added, the magnitude of $\bar{K}_m$ decreases in the upper 40 m where the water is weakly stratified, but the vertical structure of $\bar{K}_m$ remains similar to that in the homogeneous case. A significant reduction of $\bar{K}_m$ is found in the strong stratification case; $\bar{K}_m$ is significant only below 40 m where the vertical stratification is weak due to tidal mixing. The maximum of $\bar{K}_m$ is reduced to 0.02 m^2 s^{-1}, located at depths of either 45 or 60 m. Associated with the decrease of $\bar{K}_m$, the vertical friction term

$$\overline{\frac{\partial}{\partial z}K_m\frac{\partial v}{\partial z}}$$

in the along-bank direction tends to decrease in the offbank direction considerably as $\bar{K}_m$ decreases and increase at the middle depth at and near the shelf break as stratification become stronger. The maximum of

$$\overline{\frac{\partial}{\partial z}K_m\frac{\partial v}{\partial z}}$$

at the 67-m isobath is only about 0.014 × 10^{-4} m s^{-2} and is located at the surface in the homogeneous case but it increases up to 0.041 × 10^{-4} m s^{-2} and shifts down to a depth of 44 m in the strong stratification case. The decrease in $\bar{K}_m$ increases the vertical shear in the tidal flow near the bottom, and this results in an increase in the along-isobath residual current.

The generation of a tidal mixing front near the shelf break in stratified cases produces a horizontal density

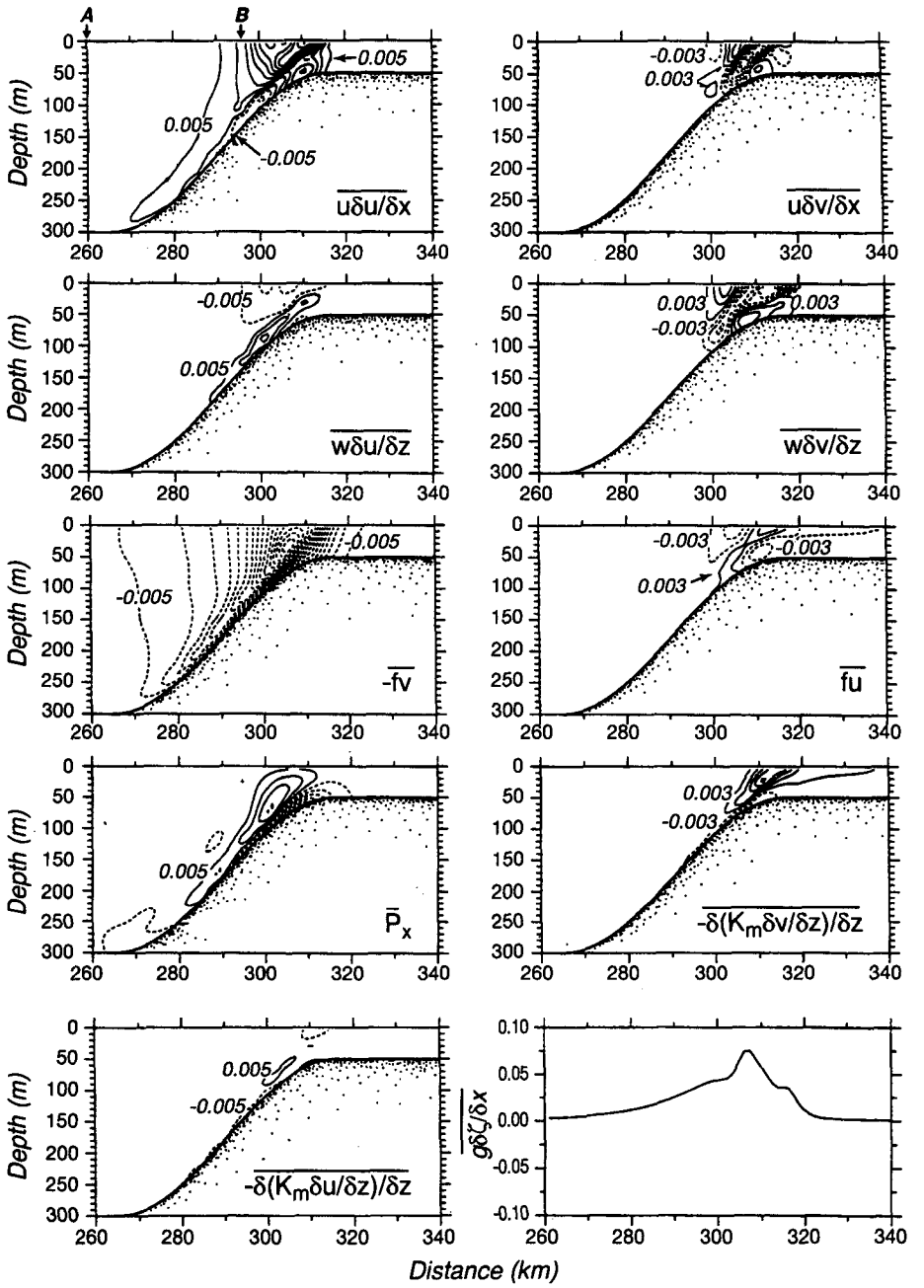

FIG. 9. Distribution of terms averaged over one tidal cycle in the cross- and along-bank momentum equations for the case of strong stratification with H_s = 50 m and l_t = 50 km (Figs. 3d,e). The unit is 10^{-4} m s^{-2}, and the contour interval is 0.01 × 10^{-4} m s^{-2} for terms in the cross-bank momentum equation and 0.005 × 10^{-4} m s^{-2} for terms in the along-bank momentum equation.

gradient, which can create an additional along-isobath residual flow. Nonlinear interactions between the barotropic and internal tidal currents as well as between internal tidal currents themselves strengthen the mean momentum flux and thus intensifies the tidal rectification process. The relative importance of these two mechanisms can be estimated using a simple scale analysis for the baroclinic pressure gradient (associated with the tidal mixing front) and horizontal advection term (associated with the nonlinear tidal interaction). The following analysis is made for the case of H_s = 50 m and l_t = 50 km.

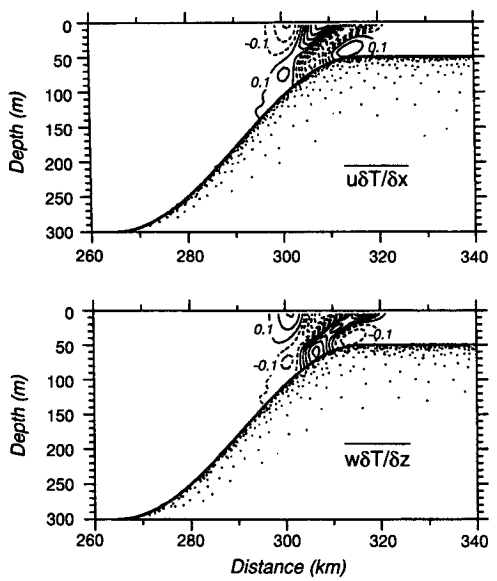

FIG. 10. Distribution of terms averaged over one tidal cycle in the heat equation for the case of strong stratification with H_s = 50 m and l_t = 50 km (Figs. 3d,e). The contour interval is 0.2 × 10^{-4} °C s^{-1}.

Near the shelf break where the maximum along-isobath residual current is located, the mean baroclinic pressure gradient is equal to

$$\left(\overline{\frac{\partial P}{\partial x}}\right) = 0.04 \times 10^{-4} \text{ m s}^{-2},$$

while the maximum horizontal advection in the cross-isobath direction is given by

$$\left(\overline{u\frac{\partial u}{\partial x}}\right)_h = 0.07 \times 10^{-4} \text{ m s}^{-2}$$

in the homogeneous case and

$$\left(\overline{u\frac{\partial u}{\partial x}}\right)_s = 0.1 \times 10^{-4} \text{ m s}^{-2}$$

in the strong stratification case. Thus, the mean baroclinic horizontal advection associated with stratified tidal rectification can be estimated as

$$\left(\overline{u\frac{\partial u}{\partial x}}\right)_b = \left(\overline{u\frac{\partial u}{\partial x}}\right)_s - \left(\overline{u\frac{\partial u}{\partial x}}\right)_h = 0.03 \times 10^{-4} \text{ m s}^{-2},$$

which is the same order of magnitude as the mean baroclinic pressure gradient. Therefore, both the tidal mixing front and the nonlinear interaction between the barotropic and internal tidal currents contribute equally to the intensification of along-isobath residual flow over the sloping bottom. It is because the nonlinear interaction due to the internal tidal generation is so important near the tidal mixing front that the semi-geostrophic balance, which holds in a linear system, is no longer valid over finite-amplitude sloping bottom topography.

5. Energy argument for tidal mixing

The numerical model results for tidal mixing are checked here using a simple energy argument. Ignoring the effects of wind mixing, horizontal friction and advection, and freshwater input from rainfall and river discharge, Simpson and Hunter (1974) found that vertical tidal mixing is predominantly controlled by the surface buoyancy flux and tidal energy dissipation. When tidal energy dissipation is strong enough to overcome the buoyancy input, the water will be vertically well mixed. Otherwise, the water will remain stratified. The transition zone between well-mixed and stratified regions is located where these two processes are balanced. This energy argument can be easily extended to our model problem as follows.

Suppose that the initial density distribution is linear with depth; that is,

$$\rho = \rho_s - \frac{\rho_b - \rho_s}{H} z = \rho_s - \frac{\rho_0}{g} N^2 z, \qquad (21)$$

where ρ_s and ρ_b are the surface and bottom densities and N is the Brunt–Väisälä frequency. After a time interval ΔT, the tidal current becomes stable and the water density is vertically mixed in a layer of depth h_m above the bottom while remaining stratified in the rest of the water column. The potential energies before and after tidal mixing are given by

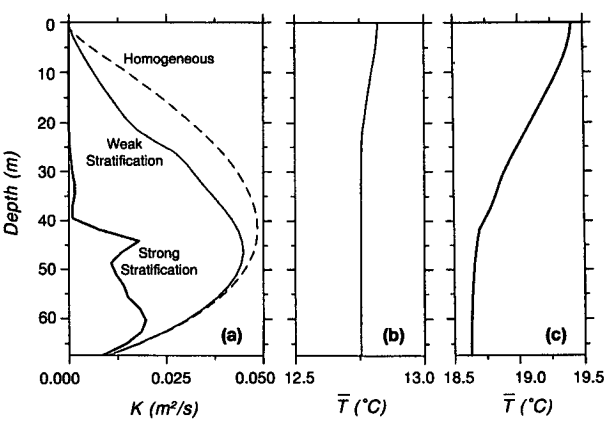

FIG. 11. Vertical distributions of the mean eddy viscosity $\bar{K}_m$ (a) and mean temperature (b and c) at the 67-m isobath near the shelf break for the homogeneous (dash line), weak (solid line) and strong (heavy solid line) stratification cases with H_s = 50 m and l_t = 50 km (Fig. 3).

$$PE_{(t=0)} = -gH^2\left(\frac{1}{2}\rho_s + \frac{1}{3g}\rho_0 N^2 H\right) \quad (22)$$

$$PE_{(t=\Delta t)} = -\frac{1}{2}\rho_s g H^2 - \frac{\rho_0}{3}N^2(H - h_m)^3 - \frac{\rho_0}{4}N^2(2H - h_m)^2 h_m, \quad (23)$$

where H is the water depth over the top of the bank. The potential energy required for the vertical mixing is thus equal to

$$\Delta PE = PE_{(t=\Delta T)} - PE_{(t=0)} = \frac{\rho_0 N^2}{12} h_m^3. \quad (24)$$

Let γ be the bottom friction coefficient and U a typical tidal current, then the average rate of dissipation of tidal kinetic energy is approximately

$$\epsilon = \overline{u_b \tau_b} = \frac{4}{3\pi}\gamma\rho_0 U^3, \quad (25)$$

where τ_b is the bottom stress and u_b a bottom velocity related to U (see Simpson and Hunter 1974). Part of this tidal kinetic energy dissipation δ is used over the period ΔT to produce the potential energy needed for vertical mixing, so

$$\frac{\rho_0 N^2}{12} h_m^3 = \left(\frac{4}{3\pi}\gamma\rho_0 U^3 \Delta T\right)\delta. \quad (26)$$

Thus

$$h_m = (16\gamma\delta\Delta T U^3/N^2\pi)^{1/3}. \quad (27)$$

This criterion implies that the thickness of the tidal mixed layer depends directly on the magnitude of the tidal current and inversely on the initial stratification. Approximate values of δ and γ can be determined from laboratory experiments and field observations. Simpson and Hunter (1974) suggested a value of $\delta = 0.0037$ for the Irish Sea, which later was derived theoretically by Hearn (1984). Usually γ is taken as 2.5×10^{-3}. Provided that these two empirical constants are applicable to our numerical experiments, this criterion should correctly predict the thickness of the tidal mixed layer found in our model experiments.

For a given tidal current and stratification, our numerical experiments show that the timescale of tidal mixing ΔT depends on the vertical resolution used in the model. As an example, Fig. 12 shows a time sequence of temperature on the top of the bank obtained using three different vertical resolutions. Although these three cases predict the same mixed layer depth, it takes about one day longer for the mixed layer temperature in the low-resolution case (KB = 31) to equal that obtained with higher resolution (KB = 61). When KB is increased further to 91, ΔT shows little difference.

Based on ΔT obtained in the experiment with higher vertical resolution, Eq. (27) predicts a mixed layer with a thickness of 40.7 m for the strong stratification case indicated in Fig. 12, where $N = 0.85 \times 10^{-2}$ s^{-1}, $U = 45$ cm/s, and $\Delta T = 13.1$ days. This value is in good agreement with the mixed layer thickness of 42 m predicted by our numerical model, implying that the Mellor and Yamada (1982) level 2 1/2 turbulent closure model and the above energy argument are mutually consistent.

6. Structure of internal tides

Time sequences of the cross-isobath and vertical velocities during one half of a tidal cycle over the upper slope are presented every 0.83 hours in Fig. 13 for the homogeneous and strong stratification cases with $H_s = 50$ m and $l_t = 50$ km (corresponding to Fig. 3). In the homogeneous case, the cross-isobath tidal current intensifies at the surface and decreases significantly in the bottom boundary layer (Fig. 13a). Correspond-

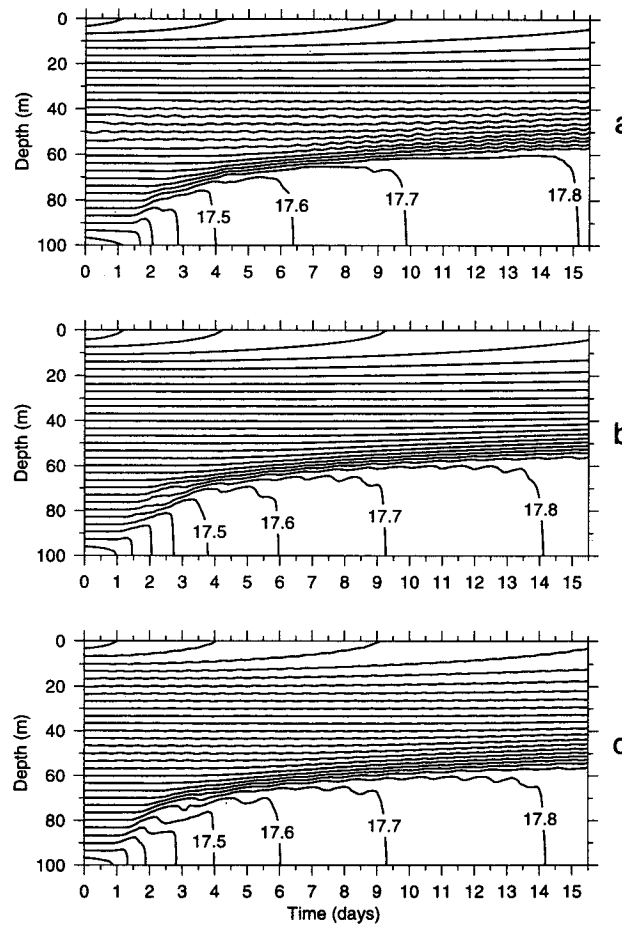

FIG. 12. Time sequence of temperature contours on the top of the bank with three different vertical resolutions (a: KB = 31; b: KB = 61; c: KB = 91). The water depth $H_s = 100$ m over the bank, and $H_d = 300$ m away from the bank. The topographic scale $l_t = 50$ km. The contour interval is 0.1°C.

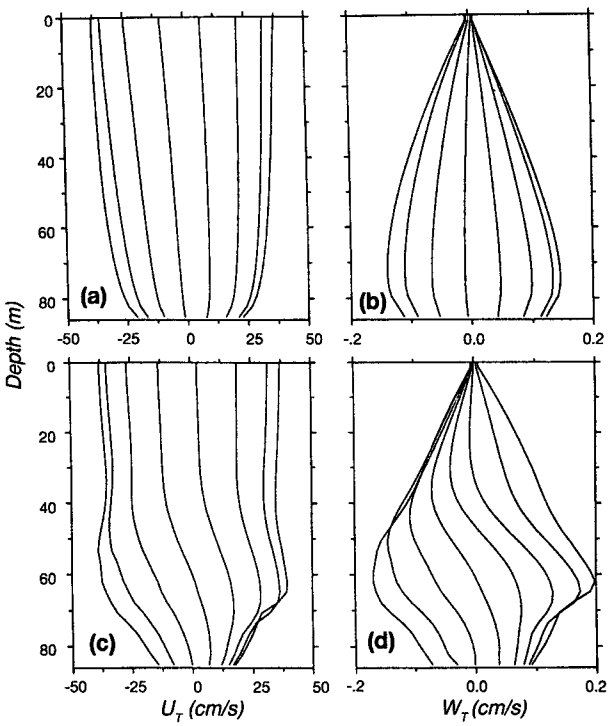

FIG. 13. Time series of cross-isobath (left) and vertical (right) tidal currents during the period of positive cross-isobath acceleration ($\partial u/\partial t > 0$) at the 84-m isobath over the upper slope for homogeneous (a and b) and strong (c and d) stratification cases (Figs. 3a,d, and e). The time interval is 0.83 hour. The water depth on the top of the bank H_s = 50 m and topographic scale l_t = 50 km.

ingly, the vertical velocity increases almost linearly with depth due to varying bottom depth except in the bottom boundary layer where the currents decrease toward the bottom (Fig. 13b). In the strong stratification case, however, the cross-isobath and vertical tidal velocities exhibit relative maxima at 30–40 m above the bottom over the slope where the vertical stratification is strongest. Such a near-bottom intensification of tidal currents on the slope is consistent with theory (Wunsch 1975) and observations on the northwestern Australian shelf (Holloway 1984).

It should be noted here that the time-dependent profiles of model tidal currents shown in Fig. 13 cannot be used directly to describe the internal tidal propagation because of the nonlinear coupling between bottom friction and stratification. The existence of the nonlinear bottom friction can induce vertical tidal motion even in a homogeneous fluid, so that vertical modes predicted from the model should include both the friction-induced barotropic and stratification-induced baroclinic modes. Since these two factors are nonlinear coupled, they cannot be directly separated from our model results. For this reason, we calculated the eigenmodes of the vertical velocity from temperature predicted from the model and the associated phase speeds for the first three modes using a fourth-order Runge–Kutta shooting method. Distribution of mean temperature, mean Brunt–Väisälä frequency, and the first three vertical velocity modes at the 300-m and 84-m isobaths on the southern side of the bank are shown in Fig. 14. These results show that the internal tide tends to decrease in wavelength and reduce its phase speed as the water becomes shallower. The phase speed of the first mode internal tidal wave is 1.95 m s^{-1} in the deep region but reduces to 0.25 m s^{-1} (during flood tide) or 0.48 m s^{-1} (during ebb tide) at the 84-m isobath. Correspondingly, the wavelength of the first internal mode is 87 km in the deep region, while it is only 11 km (during flood tide) or 20 km (during ebb tide) over the slope. It is also true for the second and third modes, implying a strong internal wave dissipation over the slope where tidal mixing is significant. These features are consistent with observations over Georges Bank (Moody et al. 1984; Marsden 1986; and Loder et al. 1992) and over the northern California continental shelf (Rosenfeld 1987).

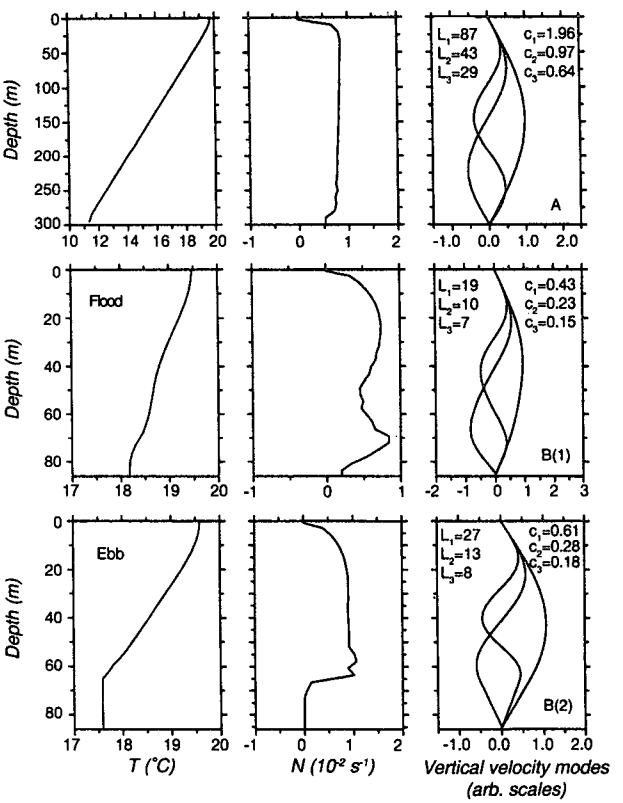

FIG. 14. Distribution of temperature (left), N (middle), and vertical velocity modes (right) at station A, 10 km away from the base of the bank, and at the 84-m isobath at station B over the upper slope. The station locations are shown at the top left in Fig. 8. The water depth on the top of the bank H_s = 50 m and topographic scale l_t = 50 km (Figs. 3d,e). The units are km for wavelength (L_i) and m s^{-1} for phase speed (c_i). B(1) and B(2) are two different cases during flood and ebb tides at the 84-m isobath, respectively.

7. Conclusions

Numerical experiments for homogeneous, weak, and strong stratification cases over different finite-amplitude symmetrical banks provide a detailed picture of stratified tidal rectification. In the homogeneous case, the tidal currents are characterized by the linear inertial–gravity wave equations modified by nonlinear advection. The nonlinear interaction of these tidal currents with the variable bottom topography generates an along-isobath jetlike residual current over both sides of the bank, which tends to increase as either the slope or height of the bank is increased. When initial stratification is included, tidal currents become modified by nonlinear advection, the baroclinic pressure gradient, and vertical friction. Internal waves at tidal and higher frequencies are generated over the sloping sides of the bank, and tidal mixing occurs in the bottom boundary layer, which leads to horizontal tidal mixing fronts near the shelf break on both sides of the bank. The resulting stratified tidal rectification leads to a subsurface intensification of the along-isobath residual current at the front and at the top of the bottom mixed layer over the slope and a cross-bank double cell circulation pattern centered at the front near the shelf break. The predicted residual currents agree well with previous analytical and numerical work in the homogeneous case and are consistent with theories of stratified tidal rectification. Model results for tidal mixing are in good agreement with a simple energy argument in which the thickness of the tidal mixed layer is proportional directly to the magnitude of the tidal current and inversely to stratification.

The basic momentum and heat balances for residual currents over a finite-amplitude symmetric bank are discussed using a diagnostic analysis. In the homogeneous case, the mean momentum is balanced between the Coriolis term and horizontal nonlinear advection in the cross-isobath direction, and among the Coriolis term, the horizontal nonlinear advection, and vertical friction in the along-isobath direction. When stratification is included, all dynamical terms except the cross-isobath vertical friction term become important in the cross- and along-isobath momentum balances, illustrating the complex nonlinear nature of stratified tidal rectification. Scaling analysis based on the model results for strong stratification clearly shows the importance of three phenomena that contribute to driving the residual flow in stratified tidal rectification over a finite-amplitude bottom topography: 1) the formation of a tide-induced front due to turbulent mixing, 2) the generation of internal waves at tidal and higher frequencies over the slope, and 3) the modification of internal friction by stratification. All three phenomena arise when the fluid becomes stratified, and their nonlinear interaction contribute to the complexity of stratified tidal rectification.

Acknowledgments. This research was supported by the National Science Foundation under Grants OCE 87-13988 and OCE 91-01034, and by the National Center for Atmospheric Research under computer time Grants 35781029 and 35781035. This research would have not been possible without the support of Alan Blumberg and Rich Signell, who allowed us to use the ECOM-si version of the Blumberg and Mellor coastal circulation numerical model and helped us understand the original three-dimensional numerical code. Also, we want to thank Ken Brink, Dave Chapman, Glenn Flierl, Glen Gawarkiewicz, Rocky Geyer, Hsiaoming Hsu, Steve Lentz, John Loder, Paola Rizzoli, Sandra Werner, and Carl Wunsch for their interest in this work and valuable comments and suggestions. We also want to especially acknowledge George Mellor, who helped us understand σ-coordinate finite-difference errors and who clarified the derivation of (A11). Anne-Marie Michael helped prepare the final manuscript, and Jack Cook helped prepare the final figures.

APPENDIX

Discussion on σ-Coordinate Errors

In the σ-coordinate system, the baroclinic pressure gradient in the cross-isobath direction is determined by

$$\frac{\partial P_b}{\partial x} = g\left(D\frac{\partial}{\partial x}\int_\sigma^0 \rho' d\sigma - \frac{\partial D}{\partial x}\int_\sigma^0 \sigma\frac{\partial \rho'}{\partial \sigma}d\sigma\right), \quad \text{(A1)}$$

where $\rho' = \rho - \bar{\rho}(x, \sigma)$, $\bar{\rho}(x, \sigma)$ is the initial reference state density transformed from the initial state $\bar{\rho}(z) = L^{-1}\int_0^L \rho\,(x, z, t = 0)dx$, L the length of the computational domain, and $D = H(x) + \zeta$ the total depth. In the ECOM-si model, P_{bx} is calculated using the finite-difference scheme

$$\frac{\Delta P_b}{\Delta x} = \frac{g}{\Delta x}\sum (D\Delta_x\rho'\Delta\sigma - \sigma\Delta_x D\Delta_\sigma\rho'), \quad \text{(A2)}$$

where Δ_x and Δ_σ are difference operators in the x and σ directions, respectively. The full expression of (A2) is given by

$$\left(\frac{\Delta P_b}{\Delta x}\right)_{i-(1/2),k+(1/2)} = \left(\frac{\Delta P_b}{\Delta x}\right)_{i-(1/2),k-(1/2)}$$

$$+ \frac{g}{\Delta x}\left\{\frac{1}{8}(\Delta\sigma_k + \Delta\sigma_{k-1})(D_i + D_{i-1})(\rho'_{i,k+(1/2)}\right.$$

$$- \rho'_{i-1,k+(1/2)} + \rho'_{i,k-(1/2)} - \rho'_{i-1,k-(1/2)})$$

$$+ \frac{\sigma_k}{2}(D_i - D_{i-1})(\rho'_{i,k+(1/2)} + \rho'_{i-1,k+(1/2)}$$

$$\left. - \rho'_{i,k-(1/2)} - \rho'_{i-1,k-(1/2)})\right\}, \quad \text{(A3)}$$

where i and k are gridpoint indices in the x and σ directions, respectively; k ranges from 2 to $KB-1$, where KB is the number of σ grid points with $\sigma_1 = 0$, $\sigma_{KB} = -1$, and $\Delta\sigma_k = (\sigma_k - \sigma_{k+1})$.

In our numerical experiments, the initial density is specified to be a linear function of z; that is,

$$\rho\,(t=0) = \rho_0 - \left(\frac{\rho_b - \rho_0}{H_d}\right)z, \qquad \text{(A4)}$$

where ρ_0 and ρ_b are the surface and bottom constant reference densities. If no forcing is imposed on the system and there is no diffusion, the perturbation density remains zero for all time, and hence no $\Delta P_b/\Delta x$ will be produced. This suggests that the σ-coordinate transformation will not generate erroneous motion over steep topography in an inviscid ocean at rest if only the perturbation density relative to a horizontal uniform state density is used to calculate the baroclinic pressure gradient. However, once diffusion occurs or the system is forced externally,

$$\rho' \neq 0, \qquad \text{(A5)}$$

which makes the fluid start to move by a nonzero baroclinic pressure gradient. For a two-dimensional model, the perturbation density becomes a function of x, z, and t, which can be written as

$$\rho' = \bar{\rho}'(z,t) + \rho''(x,z,t), \qquad \text{(A6)}$$

where the average of ρ'' in the x direction equals zero. Because $\bar{\rho}'$ is independent of x, it should not generate a horizontal pressure gradient in numerical computations. In the σ-coordinate system, however, $\bar{\rho}'$ becomes a function of x on sloping σ surfaces, so that a small computational error in the finite-difference scheme (A3) may cause an erroneous horizontal pressure gradient from a nonzero $\bar{\rho}'$ (Haney 1991).

Using Haney's analytic approach, we assume that

$$\bar{\rho}' = \rho_0' + \hat{\beta}(-z)^n \quad \text{and} \quad z = H(x)\sigma, \qquad \text{(A7)}$$

where $\hat{\beta}$ is constant and the total depth D is approximated by $H(x)$. Substituting (A7) into (A3) yields the discrete baroclinic pressure gradient

$$\left(\frac{\Delta\bar{P}_b'}{\Delta x}\right)_{i-(1/2),k+(1/2)} = \left(\frac{\Delta\bar{P}_b'}{\Delta x}\right)_{i-(1/2),k-(1/2)} + \frac{g(-1)^n}{\Delta x}\hat{\beta}\left\{\frac{1}{8}(\Delta\sigma_k + \Delta\sigma_{k-1})(D_i + D_{i-1}) \times (D_i^n - D_{i-1}^n)(\sigma_{k+(1/2)}^n + \sigma_{k-(1/2)}^n) + \frac{\sigma_k}{2}(D_i - D_{i-1})(D_i^n + D_{i-1}^n) \times (\sigma_{k+(1/2)}^n - \sigma_{k-(1/2)}^n)\right\}. \qquad \text{(A8)}$$

For $n = 1$ (a linear density perturbation), (A8) reduces to

$$\left(\frac{\Delta\bar{P}_b'}{\Delta x}\right)_{i-(1/2),k+(1/2)} = \left(\frac{\Delta\bar{P}_b'}{\Delta x}\right)_{i-(1/2),k-(1/2)} + \frac{g\hat{\beta}}{16\Delta x}(D_i^2 - D_{i-1}^2)((\Delta\sigma_k)^2 - (\Delta\sigma_{k-1})^2). \qquad \text{(A9)}$$

If the σ grid is uniform in the vertical, that is, $\Delta\sigma_k = \Delta\sigma_{k-1} = \Delta\sigma$,

$$\left(\frac{\Delta\bar{P}_b'}{\Delta x}\right)_{i-(1/2),k+(1/2)} = \left(\frac{\Delta\bar{P}_b'}{\Delta x}\right)_{i-(1/2),k-(1/2)}. \qquad \text{(A10)}$$

In the ECOM-si model, the difference scheme is designed in a way that the baroclinic pressure gradient $\bar{P}_{bx}'$ is equal to zero at the first computational level (at $\sigma_{1\,1/2}$) from the surface. This with (A10) indicates that the ECOM-si code with a uniform σ grid produces no σ-coordinate errors when the horizontal-averaged perturbation density $\bar{\rho}'$ is a linear function of z.

For higher-order ($n \geq 2$) density distributions, the finite-difference scheme will cause an error in the baroclinic pressure gradient over a sloping bottom. For example, when $n = 2$, (A8) with a uniform grid reduces to

$$\left(\frac{\Delta\bar{P}_b'}{\Delta x}\right)_{i-(1/2),k+(1/2)} = \left(\frac{\Delta\bar{P}_b'}{\Delta x}\right)_{i-(1/2),k-(1/2)} + \frac{g\hat{\beta}\Delta\sigma\Delta D\bar{D}^2}{2\Delta x}\left\{\Delta\sigma^2 - \left(\frac{\Delta D}{\bar{D}}\right)^2\sigma_k^2\right\}, \qquad \text{(A11)}$$

where $\Delta D = (D_i - D_{i-1})$ and $\bar{D} = (D_i + D_{i-1})/2$. Since $\Delta D = -\alpha\Delta x$ where α is the local bottom slope, the finite-difference error at each level vanishes as α goes to zero. Equation (A11) is similar in form to the σ-coordinate, finite-difference error in the horizontal gradient of buoyancy derived by Mellor et al. (1994). Both error expressions, their (7) and (A11), include the term

$$\left\{\Delta\sigma^2 - \left(\frac{\Delta D}{\bar{D}}\right)^2\sigma_k^2\right\}, \qquad \text{(A12)}$$

indicating that the discretization error is proportional to the difference between two terms, the first independent of k and the second increasing downward as σ_k^2. As discussed by Mellor et al. (1994), the error depends critically on which term is larger; usually in cases with realistic continental margin topography,

$$\frac{\Delta D}{\bar{D}} > \frac{\Delta\sigma}{\sigma}$$

near the bottom and the second term dominates. Since the error is additive downward, (A11) can be easily summed to obtain the baroclinic pressure gradient error in the bottom σ layer at $\sigma_{KB-(1/2)}$,

$$\left(\frac{\Delta\bar{P}'}{\Delta x}\right)_{i-(1/2),KB-(1/2)} = -\frac{g\hat{\beta}\bar{D}^2}{2}\alpha(1-\Delta\sigma) \times\left\{\Delta\sigma^2-\left(\frac{\alpha\Delta x}{\bar{D}}\right)^2\frac{(2+\Delta\sigma)}{6}\right\}, \quad \text{(A13)}$$

where $\Delta\sigma = 1/(KB-1)$. Equation (A13) demonstrates that the finite-difference error at the bottom vanishes as $\Delta\sigma^2$ and Δx^2 vanish and can be used to estimate a geostrophic error velocity V_e, where

$$V_e = \frac{1}{\rho_0 f}\left(\frac{\Delta\bar{P}'_b}{\Delta x}\right)_{KB-(1/2)}. \quad \text{(A14)}$$

The first term in (A13) tends to produce an along-isobath geostrophic flow with shallow water on the left centered at a depth deeper than where the bottom slope is maximum, while the second term tends to produce a flow in the opposite direction centered on the maximum bottom slope. In the case of steep topography where $(\alpha\Delta x)^2 \gg (\bar{D}\Delta\sigma)^2$, the second term in (A13) dominates, and V_e simplifies to

$$V_e \approx \frac{g\hat{\beta}}{\rho_0 f}\frac{\alpha^3\Delta x^2}{6}. \quad \text{(A15)}$$

Even though large error velocities can be initially generated over very steep topography, Mellor et al. (1994) show that the baroclinic pressure gradient errors will be advectively eliminated in long-time integrations.

In our numerical experiments, the standard bank topography (H_S = 50 m, l_t = 50 km) has a maximum bottom slope α = 0.008 at H = 175 m. For $\Delta\sigma$ = 0.033 (KB = 31) and Δx = 1.25 km, the two terms in (A13) are comparable in magnitude, resulting in a small maximum error velocity $V_e \approx -0.005$ cm s^{-1} at H = 270 m, where a value of $\hat{\beta}$ has been estimated from the numerical density profile to be $\hat{\beta} \approx 3.4 \times 10^{-6}$ (corresponding to $N^2 \approx 10^{-5}$ s^{-2}). For the case of the steepest topography considered here (H_S = 50 m, l_t = 12.5 km), the maximum bottom slope is α = 0.031, and the second term in (A13) dominates, resulting in a maximum error velocity $V_e \approx 0.24$ cm s^{-1} at H = 175 m.

In the real ocean, diffusion near the slope tends to mix the water in the vertical, and the condition of no-density flux into the sloping bottom requires that the density contours encounter the slope at a right angle (Wunsch 1970; Phillips 1970). Using a simple thermal boundary layer model, Wunsch (1970) estimated the thickness of the bottom diffusive layer, which is proportional to

$$\delta \sim (K_m K_H)^{1/4} N^{1/2}. \quad \text{(A16)}$$

When the fluid horizontally moves into the boundary, thermal diffusion will reduce its density and hence cause it to upwell along the slope. The vertical velocity based on Wunsch's theory is about

$$w \sim (K_m K_H)^{1/4} N^{1/2}. \quad \text{(A17)}$$

When rotation is included, an along-isobath flow can be generated in such a thermal boundary layer. Facing downstream in the direction of the current, the lighter water is located on the left (for positive f). That the maximum finite-difference error in the σ-coordinate baroclinic pressure gradient occurs at the bottom over steep topography and, in general, produces a current opposite to the true diffusive current predicted by Wunsch's theory provides us with a simple way to estimate the σ-coordinate error by checking if the numerical model flow is consistent with the predicted diffusive flow.

An example for comparison of our numerical model results with Wunsch's theory is given next. In our numerical experiments, we have taken $K_m = K_H$ for simplicity. This means that the predicted thickness of the thermal boundary layer and the vertical magnitude of vertical velocity simplify to

$$\delta \sim \sqrt{K_m/N} \quad \text{and} \quad w \sim \sqrt{K_m N}.$$

For the case of H_s = 50 m and l_t = 50 km, the numerically predicted K_m = 0.007 m^2 s^{-1} and $N^2 = 10^{-5}$ s^{-2} at a depth of 78 m, $\delta \sim 3$ m, and $w \sim 0.7 \times 10^{-2}$ cm s^{-1} there. Substituting the numerical values of K_m and N into Wunsch's formula gives

$$\delta \sim 1.5 \text{ m} \quad \text{and} \quad w \sim 0.47 \text{ cm s}^{-1},$$

which is comparable with the numerical result in the thickness of the thermal boundary layer although not in the vertical velocity. The along-isobath geostrophic velocity can be easily estimated based on Wunsch's theory. Let density outside and inside the thermal boundary layer be given by

$$\rho = \begin{cases} \rho_0 - \dfrac{\rho_b - \rho_0}{H} z \\ \qquad \text{(outside the thermal boundary layer)} \\ \rho_0 - \dfrac{\rho_b - \rho_0}{H}(z + x' \cot\alpha_1) \\ \qquad \text{(inside the thermal boundary layer)} \end{cases} \quad \text{(A18)}$$

so that the pressures at point A and B (see Fig. A1) are equal to

$$P_A = P_0 + g\rho_0\Delta h + g\frac{\rho_b - \rho_0}{2H}\Delta h^2,$$

$$P_B = P_0 + g\rho_0\Delta h + g\frac{\rho_b - \rho_0}{2H}\Delta h^2 - g\frac{\rho_b - \rho_0}{H}\Delta x \cot\alpha_1 \Delta h. \quad \text{(A19)}$$

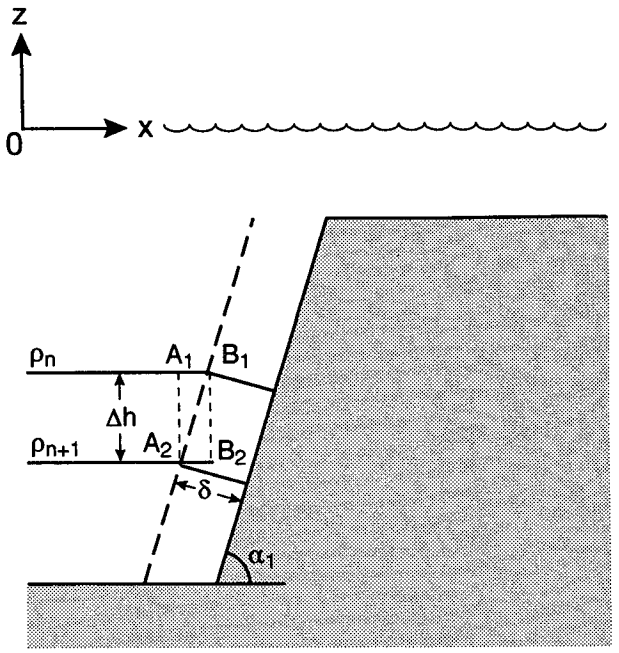

FIG. A1. Schematic density distribution in and out of the thermal boundary layer; δ is the thickness of the thermal boundary layer over the slope, α_1 is the bottom slope, and Δh is the vertical spacing between density surfaces ρ_n and ρ_{n+1}.

The along-isobath geostrophic flow is then estimated as

$$V = \frac{1}{f\rho_0}\frac{\partial P}{\partial x} = -\frac{N^2}{f}\cot\alpha_1\Delta h. \qquad \text{(A20)}$$

Since $\Delta x = \delta \sin\alpha_1$ and $\Delta h = \Delta x \tan\alpha_1$, the above equation reduces to

$$V = -\frac{N^2}{f}\delta \sin\alpha_1. \qquad \text{(A21)}$$

Taking $N^2 = 10^{-5}\ \text{s}^{-2}$, $\delta = 3$ m, and $\sin\alpha_1 = 0.005$, the alongbank bottom current due to diffusion is $V \sim -0.15\ \text{cm s}^{-1}$. In our numerical experiment, we found that $V = -0.1$ to $-0.2\ \text{cm s}^{-1}$.

This is in good agreement with the theoretical prediction, suggesting that the σ-coordinate, finite-difference error should be significantly smaller than the thermal boundary layer current in this case. Based on similar analyses made for the other numerical experiments, the numerical errors in the along-isobath velocity over the steep bottom slope in our numerical experiments are believed to be of order 0.1 cm s^{-1} or less, about 1% or less of the maximum residual current over the slope.

REFERENCES

Blumberg, A. F., 1992: A primer for ECOM-si. Tech. Report, HydroQual, Inc., Mahwah, NJ, 66 pp.

——, and G. L. Mellor, 1987: A description of a three-dimensional coastal ocean circulation model. *Three-Dimensional Coastal Models,* N. S. Heaps, Ed., 1–16.

Casulli, V., 1990: Semi-implicit finite-difference methods for the two-dimensional shallow water equations. *J. Comput. Phys.*, **86,** 56–74.

Chapman, D. C., 1985: Numerical treatment of cross-shelf open boundaries in a barographic coastal model. *J. Phys. Oceanogr.*, **15,** 1060–1075.

Chen, C., 1992: Variability of currents in Great South Channel and over Georges Bank: observation and modeling. Ph.D. thesis, MIT/WHOI Joint Program, Woods Hole, MA, 288 pp.

——, R. Beardsley, and R. Limeburner, 1995: A numerical study of stratified tidal rectification over finite-amplitude Banks. Part II: Georges Bank. *J. Phys. Oceanogr.*, **25,** 2111–2128.

Flagg, C. N., 1987: Hydrographic structure and variability. *Georges Bank,* R. H. Backus, Ed., The MIT Press, 108–124.

Galperin, B., L. H. Kantha, S. Hascid, and A. Rocati, 1988: A quasi-equilibrium turbulent energy model for geophysical flows. *J. Atmos. Sci.*, **45,** 55–62.

Garrett, C. J. R., and J. W. Loder, 1981: Dynamical aspects of shallow sea fronts. *Phil. Trans. Roy. Soc. London, Ser. A,* **302,** 563–581.

Haney, R. L., 1991: On the pressure gradient force over steep topography in sigma-coordinate ocean models. *J. Phys. Oceanogr.*, **21,** 610–619.

Hearn, C. J., 1984: On the value of the mixing efficiency in the Simpson-Hunter h/u^3 criterion. *Dtsch. Hydrogr. Z.*, **38,** 133–145.

Holloway, P. E., 1984: On the semi-diurnal internal tide at a shelfbreak region on the Australian North West Shelf. *J. Phys. Oceanogr.*, **14,** 1787–1799.

Huthnance, J. M., 1973: Tidal current asymmetries over the Norfolk Sandbank. *Estuarine Coastal Mar. Sci.*, **1,** 89–99.

Loder, J. W., 1980: Topographic rectification of tidal currents on the sides of Georges Bank. *J. Phys. Oceanogr.*, **10,** 1399–1416.

——, and D. G. Wright, 1985: Tidal rectification and front circulation on the sides of Georges Bank. *J. Mar. Res.*, **43,** 581–604.

——, D. Brickman, and P. W. Horne, 1992: Detailed structure of currents and hydrography on the northern side of Georges Bank. *J. Geophys. Res.*, **97,** 14 331–14 352.

Maas, L. R. M., 1987: Tide-topography interactions in a stratified shelf sea. Ph.D. thesis, University of Utrecht, Utrecht, the Netherlands, 241 pp.

——, and J. T. F. Zimmerman, 1989a: Tide-topography interaction in a stratified shelf sea, I: Basic equations for quasi-nonlinear internal tides. *Geophys. Astrophys. Fluid Dyn.*, **45,** 1–35.

——, and ——, 1989b: Tide-topography interaction in a stratified shelf sea, II: Bottom trapped internal tides and baroclinic residual currents. *Geophys. Astrophys. Fluid Dyn.*, **45,** 37–69.

——, ——, and N. M. Temme, 1987: On the exact shape of horizontal profile of a topographically rectified tidal flow. *Geophys. Astrophys. Fluid Dyn.*, **38,** 105–129.

Marsden, R. F., 1986: The internal tide on Georges Bank. *J. Mar. Res.*, **44,** 35–50.

Mellor, G. L., 1992: Princeton Ocean Model: User's guide for a three-dimensional primitive equation, numerical ocean model. Program in Atmospheric and Oceanic Sciences Rep., Princeton University, 35 pp.

——, and T. Yamada, 1974: A hierarchy of turbulence closure models for planetary boundary layers. *J. Atmos. Sci.*, **31,** 1791–1896.

——, and ——, 1982: Development of a turbulence closure model for geophysical fluid problem. *Rev. Geophys. Space Phys.*, **20,** 851–875.

——, T. Ezer, and L. Y. Oey, 1994: The pressure gradient conundrum of sigma coordinate ocean models. *J. Atmos. Oceanic Technol.*, **11,** 1120–1129.

Moody, J. A., B. Butman, R. C. Beardsley, W. S. Brown, P. Daifuku, J. D. Irish, D. A. Mayer, H. O. Mofjeld, B. Petrie, S. Ramp, P. Smith, and W. R. Wright, 1984: Atlas of tidal elevation and

current observations on the northeast American continental shelf and slope. *U.S. Geol. Surv. Bull.*, **1611,** 122 pp.

Phillips, O. M., 1970: On flows induced by diffusion in a stably stratified fluid. *Deep-Sea Res.*, **17,** 435–433.

Robinson, I. S., 1981: Tidal vorticity and residual circulation. *Deep-Sea Res.*, **28,** 195–212.

Rosenfeld, L. K., 1987: Tidal band current variability over the Northern California Continental Shelf. Ph.D. thesis, MIT/WHOI Joint Program, Woods Hole, MA, 237 pp.

Simpson, J. H., and J. R. Hunter, 1974: Fronts in the Irish Sea. *Nature,* **250,** 404–406.

Tee, K. T., 1979: The structure of three-dimensional tide-generating currents. Part I: Oscillating currents. *J. Phys. Oceanogr.*, **9,** 930–944.

——, 1980: The structure of three-dimensional tide-generating currents. Part II: Residual currents. *J. Phys. Oceanogr.*, **10,** 2035–2057.

——, 1985: Depth-dependent studies of tidally induced residual current on the sides of Georges Bank. *J. Phys. Oceanogr.*, **15,** 1818–1846.

——, 1987: Simple models to simulate three-dimensional tidal and residual currents. *Three-Dimensional Coastal Ocean Models,* N. S. Heaps, Ed., Amer. Geophys. Union, 125–147.

Wright, D. G., and J. W. Loder, 1985: A depth-dependent study of the topographic rectification of tidal currents. *Geophys. Astrophys. Fluid Dyn.*, **31,** 169–220.

Wunsch, C., 1970: On oceanic boundary mixing. *Deep-Sea Res.*, **17,** 293–301.

——, 1975: Internal tides in the ocean. *Rev. Geophys. Space Phys.*, **13,** 167–182.

Young, W. R., 1983: Topographic rectification of tidal currents. *J. Phys. Oceanogr.*, **13,** 716–721.

Zimmerman, J. T. F., 1978: Topographic generation of residual circulation by oscillatory tidal currents. *Geophys. Astrophys. Fluid Dyn.*, **11,** 35–47.

——, 1980: Vorticity transfer by tidal currents over an irregular topography. *J. Mar. Res.*, **38,** 601–630.

——, 1981: Topographical rectification: A comment on spectral representation. *J. Phys. Oceanogr.*, **11,** 1037–1039.